Engineering Structures 321 (2024) 118992

Contents lists available at ScienceDirect

Engineering Structures

journal homepage: www.elsevier.com/locate/engstruct

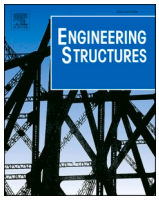

Numerical investigation on a precast bridge using GPC and BFRP reinforcements subjected to cross-fault rupture and fling step excitation

Tuan T. Ngo [a,b], Thong M. Pham [c,*], Hong Hao [a,d,**], Duong T. Tran [a], Kaiming Bi [e]

[a] Center for Infrastructural Monitoring and Protection, School of Civil and Mechanical Engineering, Curtin University, Kent Street, Bentley, WA 6102, Australia
[b] The Faculty of Engineering and Technology, Quy Nhon University, 170 An Duong Vuong Street, Binh Dinh, Viet Nam
[c] UniSA STEM, University of South Australia, Mawson Lakes, SA 5095, Australia
[d] Guangdong Provincial Key Laboratory of Earthquake Engineering and Applied Technology, Earthquake Engineering Research and Test Center, Guangzhou University, China
[e] Department of Civil and Environmental Engineering, The Hong Kong Polytechnic University, Kowloon, Hong Kong, China

ARTICLE INFO

Keywords:
Precast bridge
Earthquake excitations
BFRP reinforcements
Geopolymer concrete
Cross-fault rupture
Fling step effects
LS-DYNA

ABSTRACT

This study investigates the seismic performances of a precast bridge made of geopolymer concrete (GPC) with fibre-reinforced polymer (FRP) reinforcements subjected to cross-fault ground motions. A numerical model was developed and verified against experimental results from a previous study and then used to evaluate the bridge's performances under earthquake excitations. The study found that a simplified model was able to reliably capture the failure pattern and displacement response of the bridge, reducing simulation time significantly. Additionally, the numerical results indicated the combination of torsional and flexural cracks was the primarily damage mode of the columns, which was not observed in the experimental test. This study also revealed that while the performances of the bridge using ordinary Portland cement (OPC) and GPC were similar under low ground excitations, GPC columns were more susceptible to brittle failure under higher ground excitations due to their brittleness. The use of FRP reinforcements led to similar displacement response as steel reinforcements under low ground displacement excitation, although severe flexural and shear damages on the column of Bent 2 were observed due to the lower elastic modulus and shear resistance of Basalt FRP material than steel. To address the disadvantages of brittle GPC and low-modulus of basalt FRP reinforcements, it is suggested to reinforce GPC with fibres and/or increase stirrup ratios if green GPC and corrosion-resistant basalt FRP reinforcements are used to construct bridges for seismic resistance.

1. Introduction

The application of precast bridge structures has been increasingly becoming popular in modern bridge construction due to various benefits offered by Accelerated Bridge Construction (ABC) techniques. These benefits include a significant reduction in on-site construction time compared to conventional cast-in-situ monolithic bridges, as beams and columns are cast in a factory and then transported to the construction site for assembly. This method also minimises traffic interruptions, mitigates safety risks and environmental consequences on the construction site, and allows for effective quality control of components fabrication in the factory. Precast structures also make the effective application of new materials such as geopolymer concrete (GPC) and fibre-reinforced concrete (FRC) easier because of better-controlled mixing and curing conditions. In addition, precast structures offer easy replacement of damaged components during their service life, making them an attractive option for investors and users.

Despite numerous advantages of ABC techniques, their application has been limited mainly to low seismicity regions due to a lack of knowledge regarding the seismic performances of precast bridges under earthquake loads. This is partly due to the high cost of conducting experiments, the limitations of available equipment and software, and the insufficient experimental data available for calibrating the numerical models. Most of the current experimental studies of prefabricated bridge

* Corresponding author.
** Corresponding author at: Center for Infrastructural Monitoring and Protection, School of Civil and Mechanical Engineering, Curtin University, Kent Street, Bentley, WA 6102, Australia.
E-mail addresses: tuan@draftek.com.au (T.T. Ngo), thong.pham@unisa.edu.au (T.M. Pham), hong.hao@curtin.edu.au (H. Hao), duong.tran@curtin.edu.au (D.T. Tran), kaiming.bi@polyu.edu.hk (K. Bi).

https://doi.org/10.1016/j.engstruct.2024.118992
Received 6 February 2024; Received in revised form 12 July 2024; Accepted 15 September 2024
Available online 24 September 2024

structures focused on small-scale structural components, i.e., beams and columns. For instance, Li and Bi [1] experimentally investigated the seismic performances of segmental columns using shaking table tests under bidirectional ground motions with different peak ground accelerations. The experimental results revealed that the segmental columns were significantly twisted under bidirectional ground motions. Other previous studies [2–4] demonstrated that the energy absorption of precast segmental columns was lower than that of conventional monolithic columns because plastic hinges did not form on the segmental column under earthquake excitations. Owing to the joint opening between segments, precast segmental columns are susceptible to concrete spalling at the segment toes, which results in the main form of damage and differs from the normal flexural and shear damage observed in monolithic columns [3,5,6]. To mitigate this damage potential, various studies proposed solutions to improve the energy absorption and dissipation in segmental columns, as well as enhancing the segment strength such as the application of FRP jackets [7], energy dissipation (ED) devices [3,8], fibre-reinforced concrete (FRC) [9,10], and the use of ultra-high performance concrete [11,12].

Only a few studies [4,13–17] have conducted experiments and numerical simulations on a bridge structure, as a result, there is a lack of understanding about the seismic behaviours of the whole bridge. This is in contrast to the huge number of studies investigating the seismic behaviour of a single column or a single beam [18–21]. Sideris and Aref [13] and Sideris and Aref [14] proposed and investigated the seismic performances of a new precast bridge system including a segmental box-girder superstructure and two segmental piers. The segments were connected by unbonded tendons and rock joints. The experimental results indicated that the proposed precast bridge exhibited good seismic performances and ED characteristics. Specifically, the joint sliding and joint rocking mechanisms, along with the prestressing force in the unbonded tendons, contributed to the excellent self-centring capacity of the superstructure and enhanced ED in the columns. Johnson and Ranf [15] carried out shaking table tests on a quarter-scale two-span precast bridge to investigate the effects of incoherent motion and stiffness irregularities. The study found that the motion incoherency caused rotational displacement due to asymmetric modes, while displacement of the centre of mass was not affected by the motion incoherency. Subsequently, Choi [22] investigated the seismic behaviour of the same precast bridge tested by [23], but with a different focus on the effects of fault rupture excitations. Both these studies reported different failure modes due to various excitations, e.g., severe damage observed in Bent 3 by Johnson and. Ranf [15] and major damage reported in Bent 2 by Choi [22]. These findings highlight the need for further investigation into the bridge performances under various seismic input scenarios.

Several strong earthquakes, e.g., Northridge (1994), Hyogo-ken Nanbu (1995), Kocaeli (1999), Duzce (1999) and Chi-Chi (1999) earthquakes, showed that the effects of the motions from the near-fault (N-F) and far-field (F-F) on structural performances could be very different [4,24]. Specifically, the N-F motions exhibit a stronger and longer-period velocity pulse than the F-F motions. As a result, structures subjected to N-F motions are more likely to suffer severe damage than those subjected to F-F motions.

To minimise damage and increase the ductility of structures under N-F motions, several studies have been carried out recently. N. Abrahamson [25] revealed that rupture direction is a critical factor that affects motion in the N-F location. For instance, when the rupture direction goes toward a site, only a strong pulse may occur in N-F ground motions. Other studies [13,14,26] also investigated the effects of N-F and F-F ground motion on structures using experiments and numerical simulations. These studies concluded that N-F ground motions result in larger deformation, particularly in the vertical direction, compared to F-F ground motions. Additionally, N-F ground motions typically consist of two main components: significant velocity pulses and permanent ground displacement, which do not exist in F-F ground motions. It is noted that forward-directivity (F-D) effects usually cause significant velocity pulses whereas fling-step (F-St) effects induce prominent permanent ground deformation [4].

During an earthquake, the relative movement of the two sides of the fault can induce permanent ground displacements. The effects of fault rupture can cause bridge collapse, as seen in several earthquakes such as the 2008 Wenchuan Earthquake in China, the 1999 Chi-Chi Earthquake in Taiwan, and the 1999 Kocaeli Earthquake and Duzce Earthquake in Turkey [16]. However, there is still a lack of studies investigating the specific effects of fault rupture on whole bridges. A few studies [16,27,28] have investigated the effects of fault rupture on bridges. Saiidi and Vosooghi [16] and Choi [22] experimentally examined the impact of fault rupture on two-span precast bridges. The results revealed that the fault rupture caused local damage on the bridge and torsion cracks on the two end bents. OpenSees (Open System for Earthquake Engineering Simulation) was also used to estimate the bridge's seismic behaviour during fault rupture. However, this software has some disadvantages, such as its inability to predict bridge failure and calculate element stress and strain accurately. Therefore, it is challenging to unveil the phenomenon and confirm the failure mode based solely on observations during testing. To address this research gap and gain more insights of the bridge's behaviour during fault rupture, developing a three-dimensional (3D) finite element model using another programming is highly sought.

On the other hand, greenhouse gas emissions from producing ordinary Portland cement (OPC) contribute significantly to climate change, an alarming global issue. The production of OPC involves an energy-intensive process of calcining limestone and sintering ground materials to produce clinker, which requires burning of fossil fuels and releases substantial amounts of CO_2 into the atmosphere. If OPC is not replaced by other sustainable alternatives, it is predicted that annual CO_2 emissions from the global cement industry might reach 2.34 billion tons by 2050 [29,30]. Accordingly, GPC is a good substitute and is considered a "green" and "sustainable" material since it utilises industrial wastes, e.g., fly ash and slag, to create a new binder [31–33]. Slag is a residue left over after the refining of a targeted metal from its raw ore, while fly ash is a by-product collected from coal-fired power plants. Therefore, if GPC fully replaces OPC, it would significantly reduce CO_2 emissions released into the atmosphere [34] and promote the recycling of industrial waste to minimise environmental impacts. In addition, many studies indicated GPC has excellent acid resistance [35], good bond strength with reinforcements [36], and high flexural strength [37]. Another study [32] also demonstrated through experimental testing that the performances of GPC joints are equivalent to those of OPC joints. All the above indicated that GPC can successfully replace OPC. The use of GPC recycles industrial waste and reduces carbon footprint while still satisfying the structural requirements.

Another challenge associated with the application of ABC techniques in practice is corrosion of steel-reinforced components which can lead to bridge deterioration and require high maintenance costs. In the United States, for example, it was reported that between 1998 and 2017, the cost of maintaining and strengthening bridges due to corrosion-related issues reached $5.8 billion and $10.6 billion, respectively [38]. In fact, repairing and maintaining damaged members could sometimes cost twice as much as the original construction cost [39,40]. To address the costly corrosion issue in precast bridge construction, FRP materials can be utilised due to their desirable properties such as excellent corrosion resistance, lightweight, easy implementation, fatigue resistance, and high strength [41–44]. However, little research has been conducted to investigate the use of FRP materials in precast bridges on a large scale. Addressing this research gap could facilitate the wider application of this advanced material in bridge construction.

Considering all the limitations and research gaps discussed above, this study aims to investigate the seismic response of a precast bridge made of GPC and FRP reinforcements subjected to cross-fault and near-fault ground motions, with a focus on fault rupture and fling step effects, using numerical models developed in LS-DYNA. Due to the unavailability of relevant experimental data, the developed numerical model is

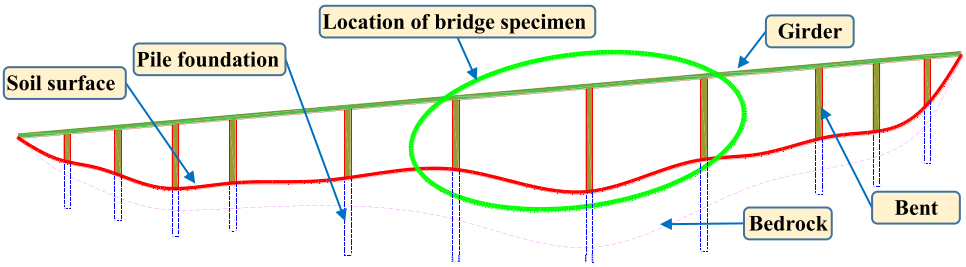

Fig. 1. Position of the bridge model in the multiple-span bridge.

Fig. 2. The bridge model on the shaking table test [22].

validated using the experimental data reported by Choi [22], which used steel reinforcements and OPC instead of GPC and FRP reinforcement. Once validated, the steel and OPC material models are replaced by Basalt FRP (BFRP) and GPC material models, respectively, to investigate the performances of bridge models using new advanced sustainable and durable materials. The constitutive models for these two materials have been verified in our previous studies and were proven to yield reliable predictions [45–49]. Two new precast bridge models with BFRP reinforcements and GPC are developed based on the validated model. The failure mode, displacement time histories, and stress-strain curve of the precast bridge with BFRP reinforcements and GPC were investigated.

2. Bridge design and construction

The adopted experimental study for validating the numerical model was a 1/4-scaled two-span precast reinforced-concrete bridge tested under cross-fault ground motion using the multiple shake table system at the University of Nevada, Reno (see Figs. 1 and 2) [22]. The precast bridge included three bents, namely Bent 1 on the left; Bent 2 in the middle; and Bent 3 on the right. Each bent consisted of a footing at the bottom, two circular columns in the middle, and a cap on the top. The total length of the bridge model in the longitudinal direction (X) was 20, 480 mm and the total heights of Bent 1, Bent 2, and Bent 3 in the vertical direction (Y) were 2661 mm, 3278 mm, and 2668 mm, respectively. It is noted that the precast bridge model was tested under spatially varying excitations in the transverse Z-direction. Details of the precast bridge, materials, and test procedure are presented in the following sections.

2.1. Details of the precast bridge

The columns in Bents 1, 2, and 3 were designed to be fixed on the top surfaces of the foundations and rigidly connected to the caps. The diameter of all the columns was identical as 305 mm whereas the length of the column on each bent varied. The length of the columns on Bent 1, Bent 2, and Bent 3 was 1520, 2440, and 1830 mm, respectively. The design of the columns was based on various standards [50–54]. Each

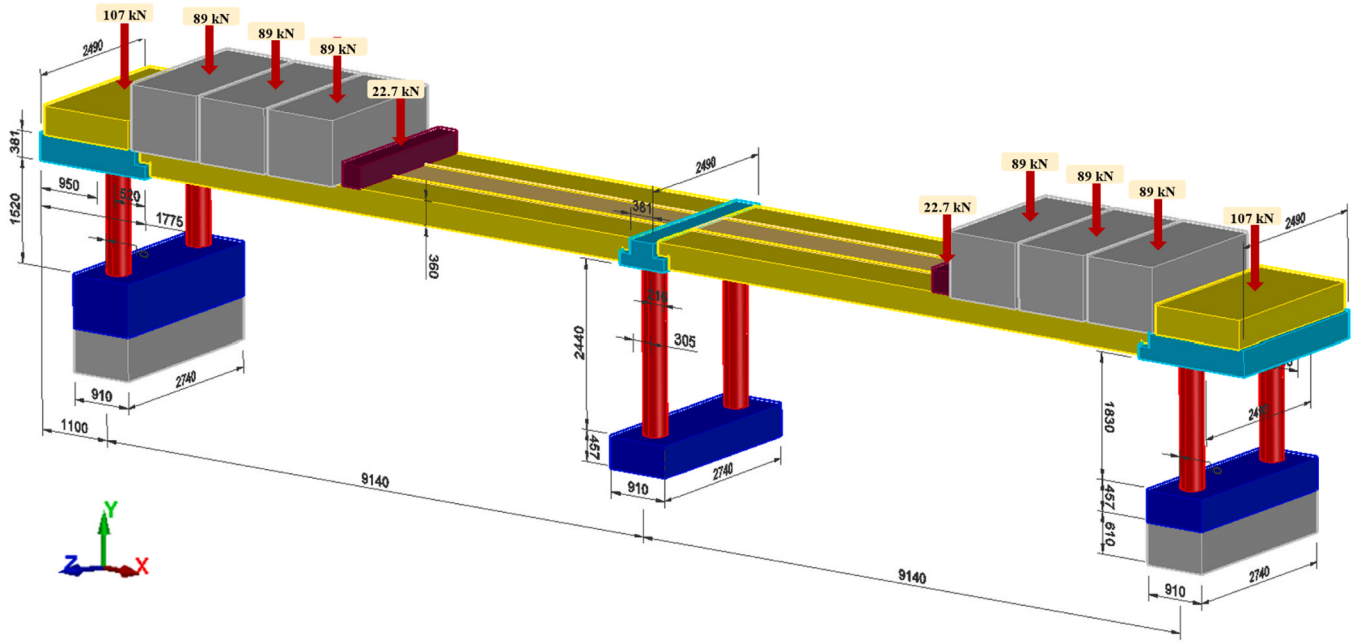

Fig. 3. 3D view of the bridge model (all dimensions are in mm).

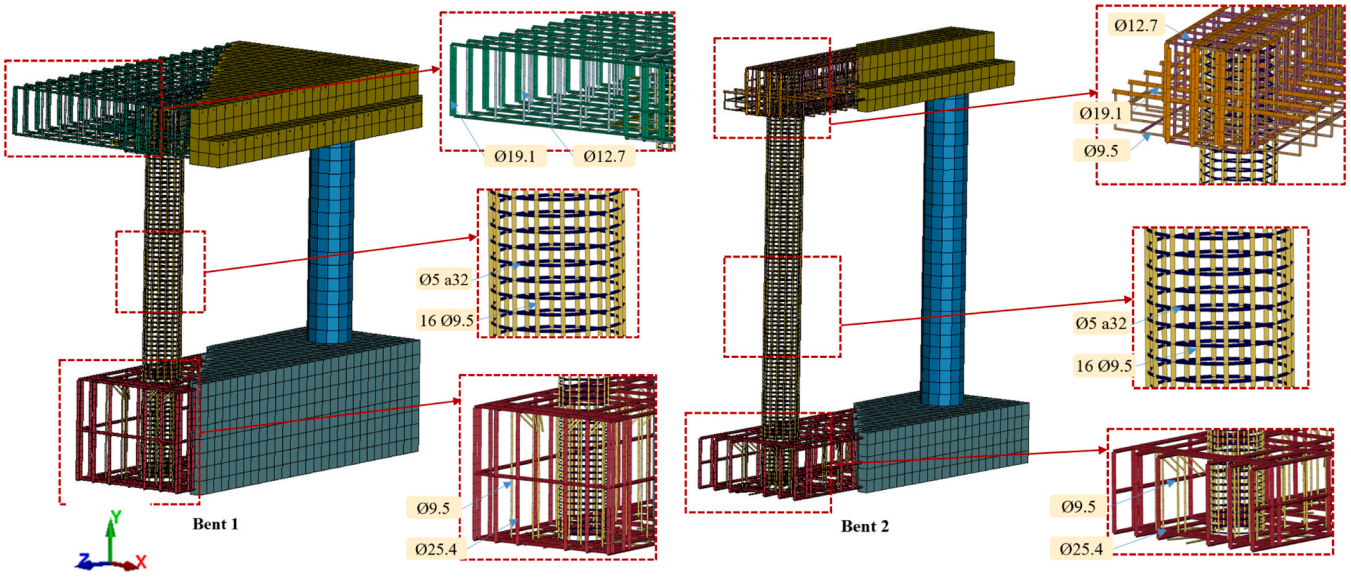

Fig. 4. Details of steel reinforcements.

Table 1
Steel reinforcement properties.

Nominal diameter (mm)	f_y (MPa)	ε_s	f_u (MPa)	ε_u
9.5	468	0.00234	692	0.19
4.8	385	0.00192	492	0.13

Note: f_y and f_u= yield strength and rupture strength of steel reinforcement. ε_s and ε_u = yield strain and rupture strain of steel reinforcement.

span consisted of three precast girders, connected together longitudinally by nine 13-mm tendons in each of the three ducts and transversely by five 32-mm threaded rods in each span. The tendons and threaded rods were prestressed at 3069 kN and 4450 kN, respectively. The application of the tendons and threaded rods was to ensure that the superstructure was formed as continuous with the same stiffness properties as multicell box girder superstructures.

The caps on the top of the bents were designed as standalone components. The objective of the shake table test was to investigate the nonlinear bridge response on the column so the strength and stiffness of the cap were designed to make sure that no cap failure occurred during the test. The dimensions of the cap are indicated in Fig. 3. The girder was specifically designed to remain in elastic during earthquake excitations. Its dimensions were 2,290-mm width, 360-mm depth, and 8,230-mm length. The girders combined with the caps on the bents form the bridge model. The beam-column joints were designed based on recommendations by California_Department_of_Transportation [53]. To ensure that the joints in the bridge model did not fail during the test, the reinforcements in the joint areas were designed to satisfy the requirements of shear resistance and joint force transfer. More details about the reinforcements and dimensions of the caps, girders, and joints can be found in Fig. 4 and the previous studies [22,23]. For the superstructure masses, owing to the scale effects, the axial stress in the columns of the prototype was lower than that of the original bridge. Hence, it was necessary to add the mass on the top of superstructures (i.e., caps and girders). The additional masses, which satisfied the requirements of the axial load index, were 54.4 tons of concrete blocks and 26.4 tons of steel blocks as indicated in Fig. 3. It is noted that the foundations in the precast bridge were not the focus of the investigation in this study so they were designed as per ACI 318–19 [54] to avoid any damage during testing. The foundation design for Bent 2 and Bent 3 was the same, while the columns on Bent 3 were shorter than those on Bent 2. To compensate for this difference, a spacer block with a height of 610 mm was added under the foundation of Bent 3. Additionally, another spacer block with a height of 617 mm was added under Bent 1 for installing the bridge model on the multiple shaking tables.

2.2. Material properties

The foundations, columns, and caps were cast separately in 3 stages. The compressive strength of concrete of the foundations, columns, and caps/girders on the test day was 45.5, 44.6, and 35.7 MPa, respectively, which was different due to different concrete batches. Three 9.5-mm steel bars and three 4.8-mm steel wires were tested. The mechanical properties of steel materials are tabulated in Table 1.

2.3. Test procedure

The low amplitude spatially varying ground displacements as illustrated in Fig. 5 were input to the shaking tables to determine the initial performance of the bridge. Afterwards, the ground displacement amplitude was gradually increased until failure occurred or reaching the displacement capacity of the shaking table. The tests were stopped after Test 6 as one of the shake tables reached its maximum displacement capacity of 356 mm. However, the numerical simulation in this study was conducted until Test 2 for verification due to the following reasons: (1) the previous study [22] did not provide sufficient input data from Tests 3–6, which makes the reliable model verification not possible, and (2) damage was observed on the bridge after Test 2. Hence, although the numerical model was validated at 0.25 peak ground displacement (PGD) (Test 1) and 1 PGD (Test 2), which covered the elastic and nonlinear inelastic responses and damage of the bridge model, they are therefore considered sufficient for model validation. Table 2 summarises the plan of running two numerical tests using LS-DYNA. The precast bridge model was subjected to multiple excitations in the transverse Z-direction (see Figs. 3 or 7). The input data of the three different ground displacement time histories to the three bents are shown in Fig. 5.

3. Numerical models of the precast bridge

LS-DYNA code was utilised to develop 3D finite element models of the precast bridge with steel/BFRP reinforcements and OPC/GPC. The experimental results from the previous study by Choi [22] were used to verify the numerical model. After validation, analyses were conducted

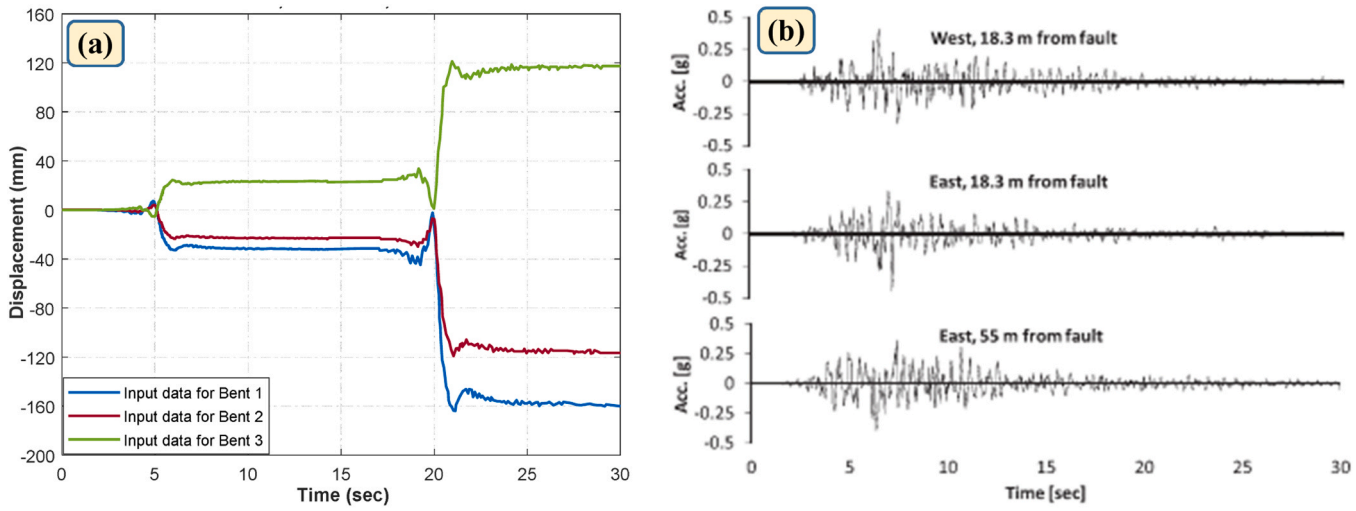

Fig. 5. Spatially varying ground displacement (a) and acceleration (b) inputs in the Z-direction.

Table 2
Plan of running the numerical model on LS-DYNA.

Test No.	Input excitations	Name of bent	PGD in Z direction (mm)
1	0.25 × PGD	Bent 1	−33.0
		Bent 2	−23.6
		Bent 3	23.4
2	1 × PGD	Bent 1	−130.1
		Bent 2	−94.5
		Bent 3	96.8

to investigate the performances of the precast bridge made of GPC and FRP materials subjected to cross-fault earthquake excitations. In addition, the numerical results were used to examine some phenomena which could not be explained based on the experimental results.

3.1. Element properties and contact mechanism

The element types, mesh sizes, contact mechanisms, and method to apply prestressing forces for the tendons and threaded rods are presented in this section. The shape of bridge models is shown in Fig. 7.

3.1.1. Element types

Constant stress solid 8-node elements were used to simulate concrete, steel blocks, and steel plates in the numerical models. Meanwhile, steel and BFRP reinforcements (i.e., longitudinal reinforcements and stirrups) were modelled by Hughes-Liu two-node beam elements with 2 × 2 Gauss quadrature integration. A mesh convergence test on various mesh sizes (40, 50, 80, 100, and 120 mm) was conducted to determine the optimal mesh size with acceptable predictions and reasonable computation time (see Fig. 6). 80-mm mesh size was considered for the critical parts such as columns, foundations, caps, and spacer blocks while a big mesh size of 300 mm was chosen for concrete blocks, steel blocks, and girders. The mesh size of reinforcements was chosen as the same as crucial parts of 80 mm to ensure good bonding between reinforcements and concrete. The tendon and threaded rods originally were modelled by constant stress 8-node solid element and Hughes-Liu two-node beam element, respectively. However, the simulation time was too long, up to one month to run a case of the bridge model while they were not the primary focus. Hence, the prestressing forces on

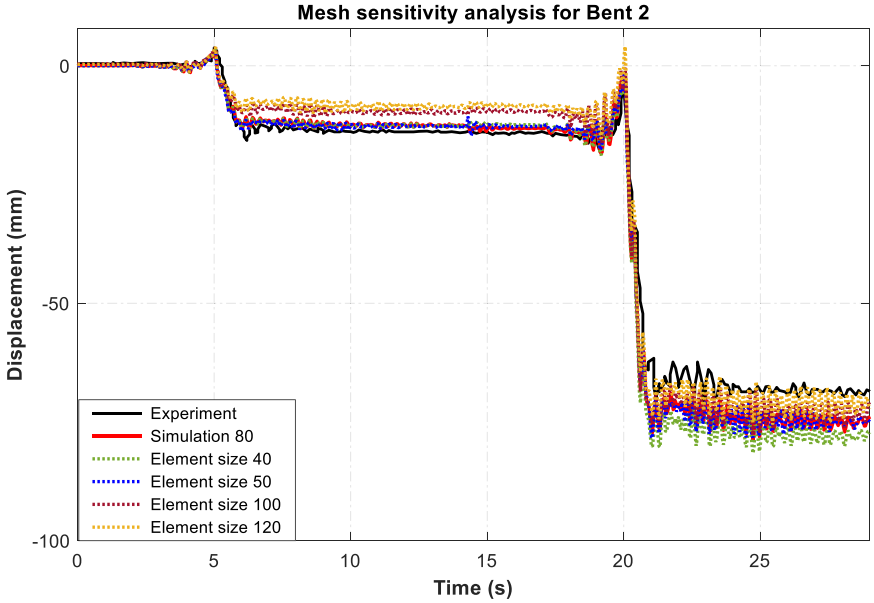

Fig. 6. Typical mesh sensitivity analysis for Bent 2.

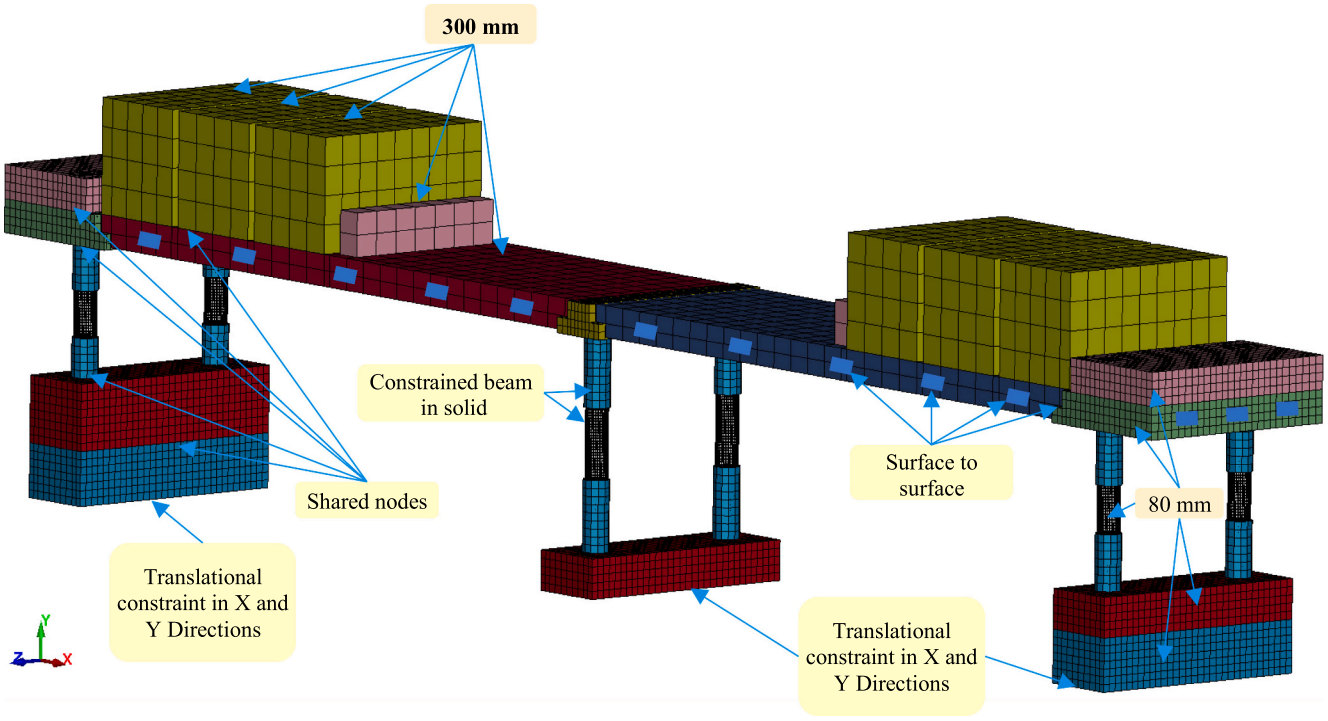

Fig. 7. Details of mesh size and contact mechanism.

Table 3
Key parameters of the modified 45 MPa GPC material model.

MID	RO	PR					
18	2.351e−09	0.19					
FT	AO	A1	A2	B1	OMEGA	A1F	
3.8050001	13.302	0.4463	0.001796	0.6	0.5	0.3334	
Slambda	NOUT	EDROP	RSIZE	UCF	LCRATE	LOCWIDTH	NPTS
100	2	1	0.03937	145	11	30	0.0
Lambda1	Lambda2	Lambda3	Lambda4	Lambda5	Lambda6	Lambda7	Lambda8
0	8e−06	2.4e−05	4e−05	5.6e−05	7.2e−05	8.8e−05	3.2e−04
Lambda9	Lambda10	Lambda11	Lambda12	Lambda13	B3	A0Y	A1Y
5.2e−04	5.7e−04	1	10	1e+ 10	1.15	10.675	0.625
eta1	eta2	eta3	eta4	eta5	eta6	eta7	eta8
0	0.85	0.97	0.99	1	0.99	0.97	0.5
eta9	eta10	eta11	eta12	eta13	B2	A2F	A2Y
0.1	0	0	0	0	1.35	0.002628	0.005722

EOSID	**GAMA**	**EO**	**VO**	
1	0.0	0.0	1	
EV1	**EV2**	**EV3**	**EV4**	**EV5**
0.0	−0.0015	−0.0043	−0.0101	−0.0305
EV6	**EV7**	**EV8**	**EV9**	**EV10**
−0.0513	−0.0726	−0.0943	−0.174	−0.208
C1	**C2**	**C3**	**C4**	**C5**
0.0	25.609541	55.827271	89.636803	170.30440
C6	**C7**	**C8**	**C9**	**C10**
256.87140	364.43280	557.53113	3255.0410	49,785,991
T1	**T2**	**T3**	**T4**	**T5**
0.0	0.0	0.0	0.0	0.0
T6	**T7**	**T8**	**T9**	**T10**
0.0	0.0	0.0	0.0	0.0
K1	**K2**	**K3**	**K4**	**K5**
1.707E+ 04	1.707E+ 04	1.731E+ 04	1.818E+ 04	2.163E+ 04
K6	**K7**	**K8**	**K9**	**K10**
2.509E+ 04	2.854E+ 04	3.116E+ 04	7.010E+ 04	8.536E+ 04

Note: RO= Mass density.
PR= Poisson's ratio.
FT= Relative tensile strength.
RSIZE= Length unit conversion factor.
UCF= Tress unit conversion factor.
Other parameters are provided found in the LS-DYNA materials Manual.

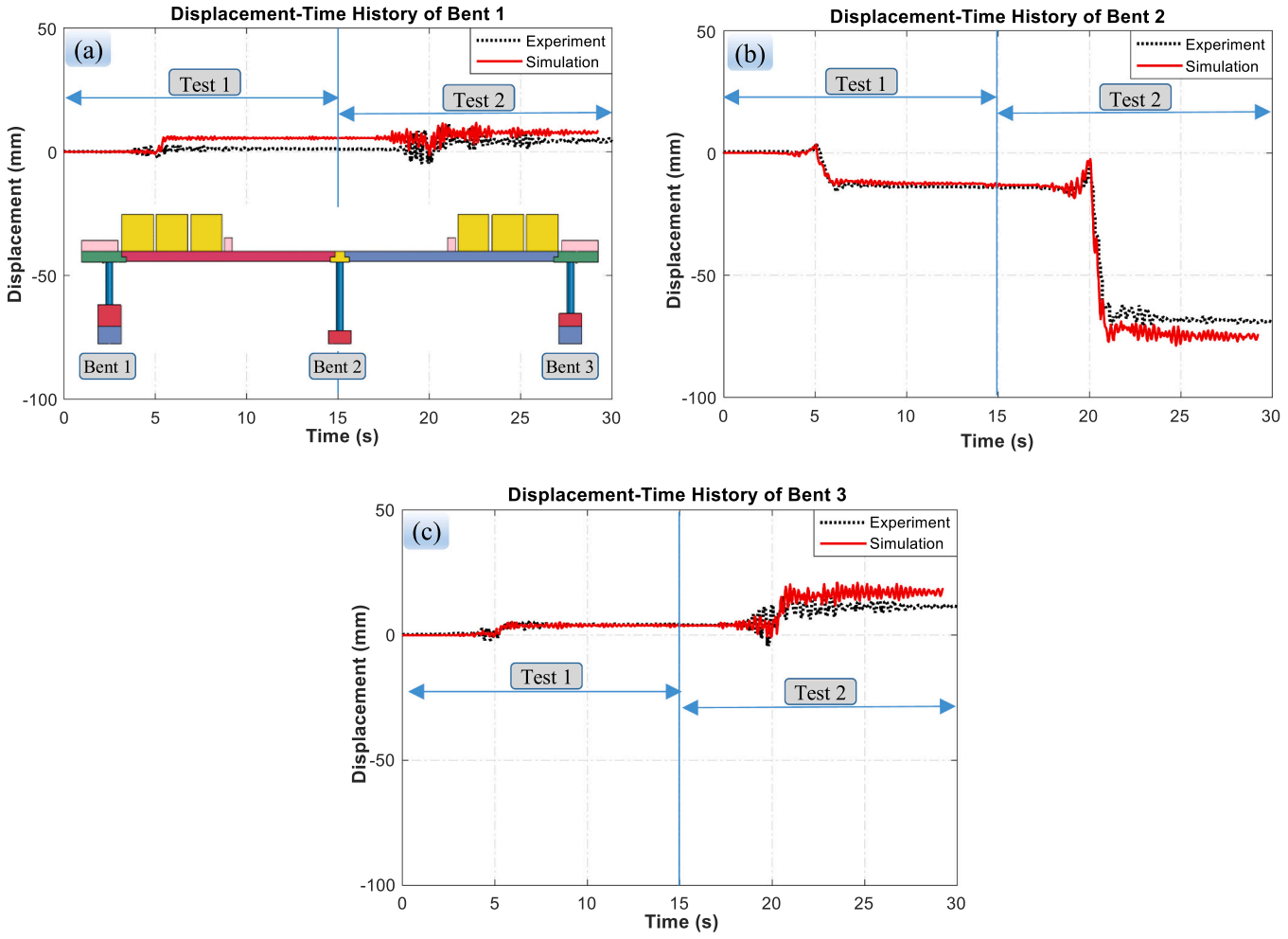

Fig. 8. Comparisons between numerical simulation and test data.

tendons and threaded rods were replaced by applying pressure on the steel plates. With this simplification, the simulation time was significantly reduced from one month to a week. The above simplification may compromise the prediction accuracy, especially in the local areas near the posttension tendons, but the numerical results of the global bridge responses later show acceptable predictions compared to the testing results.

3.1.2. *Contact mechanisms and boundary conditions*

The reinforcements (slave beam elements) were embedded into concrete (master solid elements) by the coupling-constrained method [48,55]. The keyword *CONSTRAINED_BEAM_IN_SOLID was used for the above method. The keyword *CONTACT_AUTOMATIC_SURFACE_TO_SURFACE was employed for contact interfaces between the girders and caps, steel plates and caps/girders. The coefficient of friction of 0.6 was adopted for the contact between the girders and caps while those for the contact between steel plates and caps/girders were 0.6 and 0.5, respectively [56]. In addition, based on the information from the previous study [22], the translational constraint in X and Y directions was applied to the bottom surfaces of the foundation (Bent 2) and spacer blocks (Bents 1 and 3). Meanwhile, no translational constraint was adopted to the Z direction so that the input ground displacement time histories can be applied to this direction only. The keyword *BOUNDARY_PRESCRIBED_MOTION_SET was used to apply the ground motion.

3.2. *Material model*

3.2.1. *Material model of OPC and GPC*

The constitutive models in LS-DYNA are very abundant and suitable for investigating structural responses subjected to various loading conditions such as seismic, static, impact and blast loads. Some material models could be used for modelling concrete subjected to earthquake excitations in LS-DYNA such as *MAT_CONCRETE_DAMAGE (MAT_072), *MAT PSEUDO TENSOR (MAT_016), *MAT CONCRETE DAMAGE REL3 (MAT_072R3). Among various concrete material models, this study adopted MAT_072R3 material model to simulate the behaviour of conventional concrete in terms of shear damage, strain rate effect, plasticity, and strain softening. The accuracy of MAT_072R3 in predicting the structural behaviour under earthquake has been verified in previous studies [17,57]. However, the MAT_072R3 also has a disadvantage of not showing the crack formation and crack propagation in detail. It is because the MAT_072R3 predicts the material damage based on the continuum damage mechanics, not crack details as fracture mechanics [55]. Hence, MAT_072R3 can only predict the damaged locations but not crack patterns.

Regarding the GPC material model, this study adopts the modified MAT_072R3 model for GPC material in the previous studies [45–47]. It is noted that this modified material model for GPC was verified under many loading conditions, e.g., by Huang and Chen [47], Tran and Pham [58] and Huang and Chen [46] under static and impact loads and Li and Bi [45] under seismic loads. The results of the previous studies [45–47] indicated that the modified model for GPC material could reliably

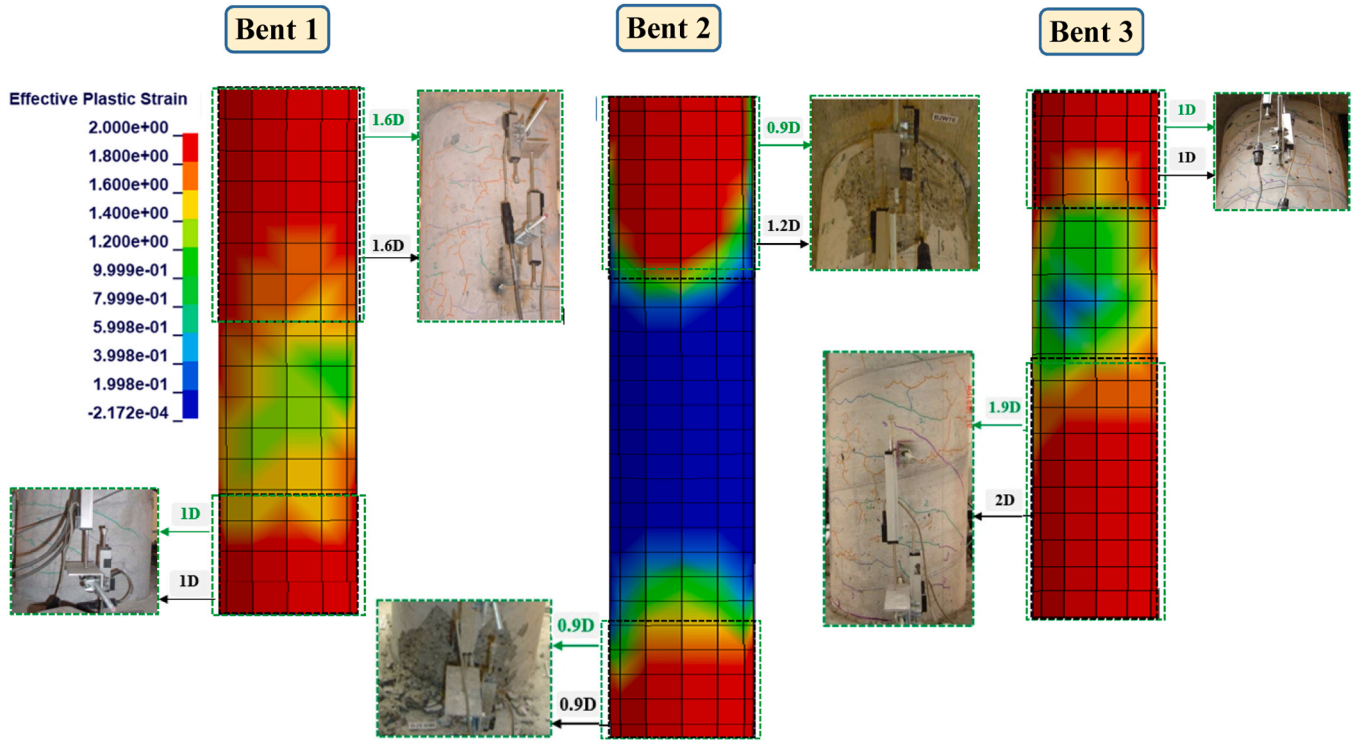

Fig. 9. Comparisons of failure patterns between numerical simulation and experiment. **Note:** the black and green dashed rectangles indicate the comparison of the damaged areas between numerical and experimental results, with respect to the diameter of the column, D.

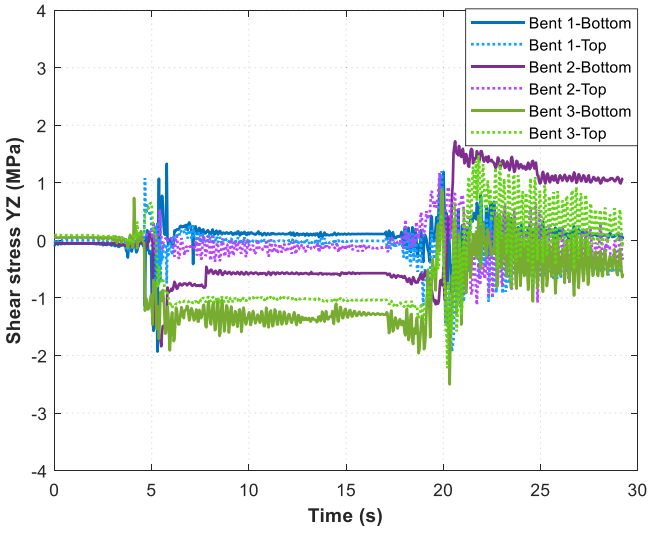

Fig. 10. Shear stress at the critical section: The column top and bottom (Unit: MPa).

capture the failure mode and dynamic response time histories of GPC structures. It indicates that the modified GPC material model is valid and reliable. Some assumptions have been adopted when deriving GPC material model. For example, given that OPC and GPC exhibit similar yield and peak compressive strengths, most parameters were kept at their default values. However, since the parameters a_{1r} and b_1 depend on the residual strength and the damage evolution of concrete, respectively, they significantly influence the concrete's softening behaviour under compression. Consequently, adjustments to these two parameters, a_{1r} and b_1, are necessary. The main modification parameters of 45 MPa GPC are summarised in Table 3. For brevity, the detailed information of the modified GPC model is not repeated herein.

3.2.2. Steel and BFRP material models

An elastic-plastic material model using the keyword *MAT_PLASTIC_KINEMATIC (MAT_003) was utilised for both steel and FRP reinforcements. It should be noted that FRP material shows brittle failure and does not experience plastic deformation. In this study, for simplicity, the same material model MAT_003 was adopted to model both FRP and steel with their respective modulus and the yield stress of FRP was specified as 1200 MPa, the same as its ultimate strength. With this specification, the FRP reinforcements had only elastic performances during numerical simulation [56]. An elastic material model with the keyword *MAT_ELASTIC (MAT_001) was used for steel plates and steel blocks. It is noted that the elastic material model MAT_001 was also utilised for the foundation, girder, cap and concrete blocks because these components were designed so that no failure occurred during the test.

3.3. Model validation

Simulating the performances of the considered bridge models using LS-DYNA, including local damage, is a challenging task due to the large number of elements involved. It can take up to a month to run a single case if all details of the experimental model are adopted without simplification. To overcome this issue, a simplified model was developed in LS-DYNA in which the tendons, threaded rods, and holes were not modelled in detail while their functions were equivalently modelled to obtain reliable predictions of the bridge structure. In the numerical model the tendons and thread rods were not included, but the equivalent pressure they imposed on concrete were considered, resulting in a more computationally efficient simulation. The simulations were carried out continuously using the spatially varying ground displacements as illustrated in Fig. 5 as inputs. Test 1 (0.25 PGD) was conducted from 0 to 15 s (s) whereas Test 2 (1 PGD) was conducted from 15 to 30 s as in the laboratory tests. To evaluate the accuracy of the numerical model, the simulation results were compared with the experimental results

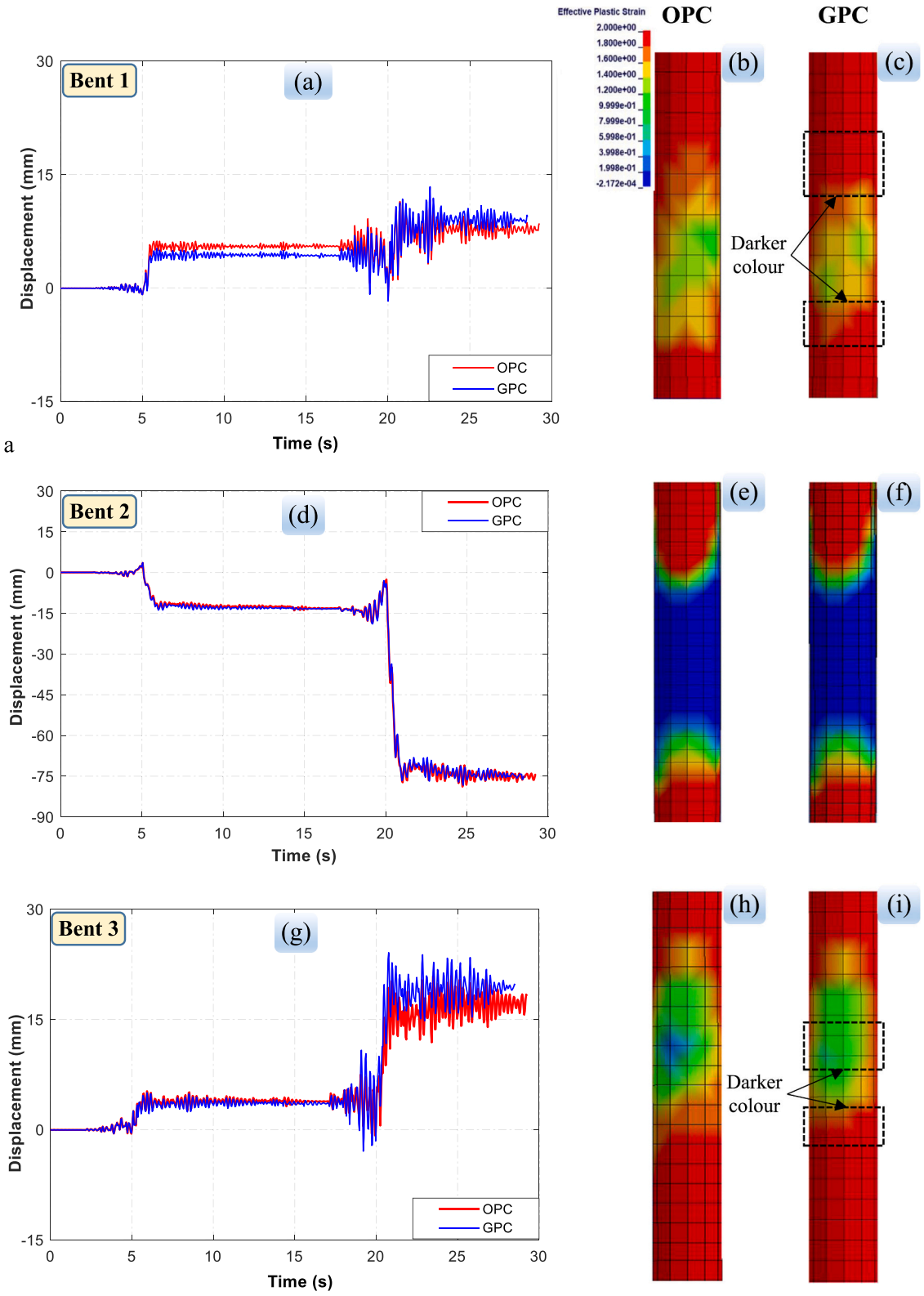

Fig. 11. Comparison of displacement and plastic deformation between OPC and GPC.

regarding the failure mode and displacement time histories.

3.3.1. *Displacement time history*

Fig. 8 illustrates the comparisons between the displacement time histories obtained from the numerical simulation and the test results. It was found that the numerical simulation can successfully replicate the experimental tests in terms of the response trend. Differences in the peak and residual displacements between experimental and numerical results were observed. For example, a minor variation of the peak and residual displacements was recorded on Bent 2 and Bent 3 from 0 to 15 s, but this difference increased to about 9.5 % from 15 to 30 s. These observations indicate the numerical model can well predict the elastic responses of

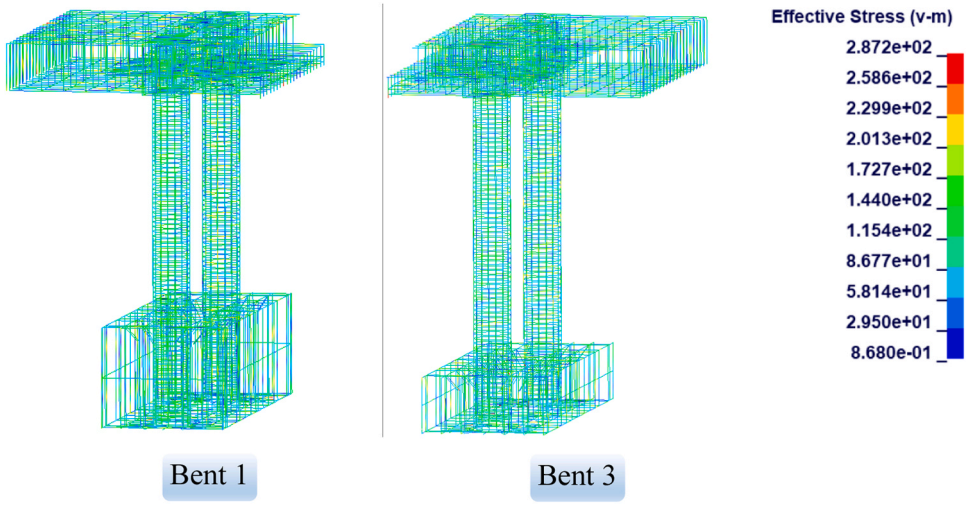

Fig. 12. Effective stress of steel reinforcements in Bents 1 and 3 (unit: MPa). **Note:** maximum tensile stress on the reinforcement is 287.2 MPa.

Table 4
Parameters of the material models.

Parts	Material models in LS-DYNA	Parameters	Values	Units
Concrete (Column)	072R3-CONCRETE_DAMAGE_REL3	RO (Mass density)	2400	kg/m^3-
		PR (Poisson's ratio)	0.2	MPa-
		A0 (Compressive strength)	45	-
		RSIZE (Length unit conversion factor)	0.03937	
		UCF (Stress unit conversion factor)	145	
GPC (Column)		SeeTable 3	SeeTable 3	-
Steel Rebars	003-PLASTIC_KINEMATIC	Mass density	7800	kg/m^3
		Young's modulus	200	GPa
		Poisson's ratio	0.3	-
		Yield stress	468	MPa
		ETAN (Tangent modulus)	1000	-
Stirrups on column	003-PLASTIC_KINEMATIC	Mass density		kg/m^3
		Young's modulus	7800	GPa
		Poisson's ratio	200	-
		Yield stress	0.3	MPa
		ETAN (Tangent modulus)	385	-
			1000	
BFRP rebars	003-PLASTIC_KINEMATIC	Mass density	2000	kg/m^3
		Young's modulus	55	GPa
		Poisson's ratio	0.25	-
		Ultimate strength	1200	MPa
		ETAN (Tangent modulus)	-	-
Foundations, girders, cap, concrete block	001-ELASTIC	Mass density		kg/m^3
		Young's modulus	2400	GPa
		Poisson's ratio	30.8	-
			0.2	
Steel plates, steel blocks	001-ELASTIC	Mass density		kg/m^3
		Young's modulus	7800	GPa
		Poisson's ratio	200	-
			0.3	

Notes: '-' means not applicable.

the bridge when the excitation intensity is small, but has some errors when plastic deformation and damage occur in the bridge structural components when subjected to large ground excitations. This is because of the simplification in modelling the posttensioning tendons and threaded rods as described above. Under strong ground excitations, concrete damage is likely to initiate at weak sections and locations with stress concentration owing to the application of posttensioning forces. These were not captured by the simplified modelling approach in this study as it equivalates the posttensioning forces and apply them uniformly on the concrete. Other possibilities that might induce these discrepancies also include inevitable variations in material properties and observed slip of spacer which is further discussed. Nonetheless, the differences are less than 10 %, which is acceptable considering such a large numerical model. It is obvious that the numerical residual displacement in the initial stage (0–15 s) of Bent 1 was higher than the experimental results. This is because there was a slip between the spacer and the shaking table in the test as stated in [1] but it was not modelled in the simulation. The spacer was bolted to the shaking table to accommodate the elevation difference of the multiple bridge supports in the shaking table tests. Slip was observed in the test but the actual slip data was not provided in [1]. It is noted that the relative displacement was calculated as the difference between the top and bottom displacements. Hence, the presence of slip resulted in lower peak and residual displacements in the experimental results compared to the numerical results without slip. Especially, the effect of slip on the relative displacement was particularly prominent in Bent 1, which had the

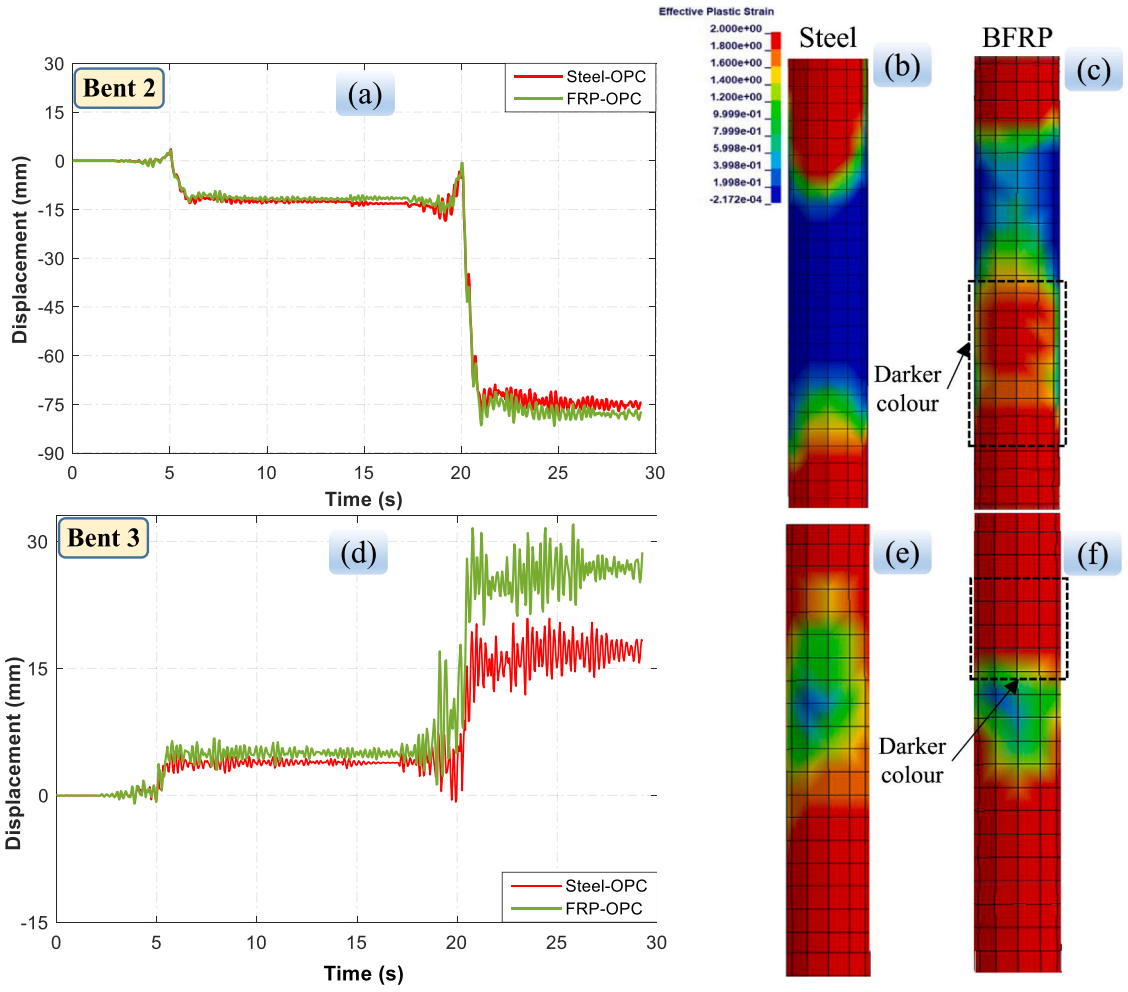

Fig. 13. Comparisons of displacements and effective plastic strain between BFRP and steel reinforcements.

lowest residual displacement (1.28 mm) compared to Bent 2 (−13.75 mm) and Bent 3 (4.2 mm) during the first 15 s. This is because when the bridge response is large, the existence of foundation slip becomes less prominent.

3.3.2. *Failure modes*

In general, the concrete damage contour (i.e., effective plastic strain) from the numerical simulations agreed well with the observed concrete cracks on the columns of Bents 1–3 in the experiment. Specifically, the numerical model successfully predicted the flexural damage observed on the columns of Bent 2. In Fig. 9 (Bent 2), the numerical model displayed red contour at the top and bottom of the column, which was consistent with the observed flexural damage during the experiment. To prove that the damage on the columns of Bent 2 was primarily governed by bending moment, a *P-M* interaction curve was derived according to details of the cross-section of column, reinforcements, and mechanical properties of steel and concrete. The numerical results revealed that the bending moments at the top and bottom of the column of Bent 2 exceeded the estimated flexural capacity of the columns based on the *P-M* interaction curve. In particular, the estimated bending moment capacity of the column was 83.4 kN.m, whereas the maximum bending moment at the column top of Bent 2 was 90.3 kN.m while the actual shear force did not reach its estimated shear capacity yet. Hence, it can be concluded that the damage on the column of Bent 2 was mainly caused by the large bending moment with flexural cracks, the same conclusion was also given in the previous study based on experimental observations [22].

Meanwhile, a combination of bending and torsional moments caused damage to the column of Bents 1 and 3. The numerical model showed that the bending moment on these columns reached the bending moment capacity of the column, i.e., 83.4 kN.m. In addition, the cross-section of the columns and the stirrup areas in these columns were not sufficient to resist the torsional moment. For instance, the required stirrup area was 93 mm^2/mm according to ACI 318–19 [54] whereas the actual area of the stirrup in the column was only 1.3 mm^2/mm. Hence, the numerical simulation results demonstrated that torsional and flexural cracks governed the main damage of the column on Bents 1 and 3. This finding aligns with the conclusion for Bent 3 but differs from the conclusion for Bent 1 in the previous study [16]. For Bent 1, only torsional cracks were reported in the experiment. This is because these flexural cracks were small, so they may have been assumed to be torsional cracks. This highlights a limitation of relying solely on visual observations in experiments. In addition, the stress states within concrete joints are complex. Determining the exact cause of damage can be challenging. Numerical simulations offer a convenient way to examine these stress states. As a result, this current study helps to clarify the observations made in the test. It is noted that the difference in damage between Bents 1,3 and Bent 2 was attributed to several factors, including different input data for each bent and differences in column lengths. Specifically, the column lengths of Bents 1 and 3 were 1525 and 1835 mm, respectively, whereas that of Bent 2 was 2442 mm, as described above.

To assess whether the columns had sustained shear damage, the maximum shear stress at the critical sections on the columns of Bents 1, 2, and 3 was plotted and compared with the nominal shear strength of

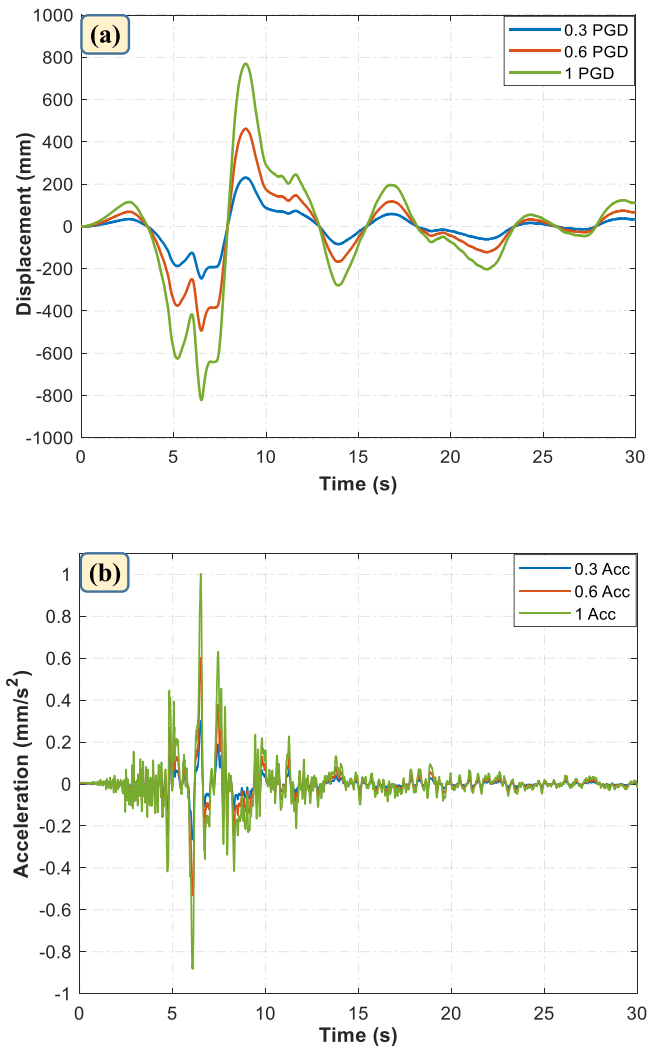

Fig. 14. Different input data for the bridge model, (a) Displacement; (b) Acceleration [4].

concrete. As can be seen in Fig. 10, the maximum shear stress in these three Bents was 2.5 MPa which was smaller than the nominal shear strength of concrete (3.6 MPa). Therefore, it is evident from the analyses that the columns in Bents 1, 2, and 3 did not suffer shear damage. The numerical model successfully predicted the damage patterns and was validated with the experimental observations.

4. Sensitivity analysis

4.1. Performances of the precast bridge under low earthquake excitations

4.1.1. Performances of bridge using GPC vs OPC

The use of GPC instead of conventional concrete (OPC) has become a popular trend in modern construction due to its numerous benefits, as outlined in the introduction. However, research investigating the performances of GPC bridges under earthquake excitations is still scarce. Consequently, the application of GPC in bridges is very limited or does not exist yet. To explore the possibility of using this sustainable green construction material in bridge construction, numerical simulations of the responses of a precast bridge constructed with GPC are carried out. This is the first study of its kind to investigate the performances of the GPC precast bridge, and as such, there are no existing experimental results of a precast bridge model cast in GPC in the literature, nor is there a GPC material model available for use in finite element software. To address these issues, this study adopts the modified OPC material model for GPC from the previous studies [45–47] and then applies this GPC material model to the verified model presented in Section 3.3. This GPC material model has been verified on different structures under dynamic loads (e.g., impact and seismic loads) so it is reliable for use in the precast bridge model. In the verified bridge model presented in Section 3.3, only the OPC material model was replaced with the modified GPC material model while other parts remain unchanged. It should be noted that, to focus on the concrete material, both numerical models used steel reinforcements.

Fig. 11 shows the performance comparisons between the precast bridges made of OPC and GPC in terms of displacements and damage scalar (effective plastic strain). In general, the performances of OPC and GPC in Bents 2 and 3 were almost identical in the initial state with the low ground excitation (0.25 PGD). For instance, during the first 15 s of low ground excitation, the peak relative displacement and residual displacement of the OPC columns in Bent 2 were 13.2 mm and 12.6 mm, respectively, while the corresponding values of GPC columns were slightly higher at 13.8 mm and 13.1 mm, respectively. Similarly, in Bent 3, the peak relative displacement and residual displacement of OPC columns were 5.2 mm and 3.9 mm, respectively, while those of GPC were slightly lower at 5.0 mm and 3.7 mm, respectively. Overall, the differences in displacement between OPC and GPC columns were marginal because these bents showed elastic performances in the initial state, indicating comparable performance of GPC and OPC in this stage. This observation was also reported in previous studies on beam-column joints under cyclic loads [32,33].

When the input of the earthquake excitations was increased from 0.25 PGD to 1 PGD, the GPC columns in Bents 1 and 3 exhibited higher peak relative displacement and residual displacement compared to their OPC counterparts. For instance, the residual displacements of the GPC columns in Bents 1 and 3 were approximately 15 % and 12 % greater than that of the corresponding OPC columns, respectively. This result can be attributed to two main reasons:

(1) Because the axial stress in reinforcements of these bents did not reach their yield strength (Fig. 12), concrete dominated damage of Bents 1 and 3. Meanwhile, GPC was reported to exhibit brittle damage under intensive loads in previous studies [32,59]. This brittleness could cause more severe damage, leading to higher peak and residual displacements of GPC as compared to OPC. This explanation was confirmed by comparing the damage shown in Fig. 11. The red colour on the top and bottom of the GPC columns occurred earlier on Bents 1 and 3, compared to the OPC columns. Additionally, a darker red colour was observed on the GPC column, compared to the OPC column (Fig. 11).

(2) The elastic modulus of GPC (20 GPa) is significantly lower than that of OPC (32 GPa), estimated based on A. Noushini, F. Aslani [60] and ACI 318–19 [54], respectively. The lower elastic modulus resulted in a lower stiffness of GPC columns compared to OPC columns, leading to higher peak displacements of the GPC column under seismic loads. This phenomenon was also observed in the previous study when comparing the deformation of GPC vs OPC beam-column joints under cyclic loads [32]. Notably, despite GPC having a smaller modulus compared to OPC, the displacement of GPC columns under smaller excitations was either similar in Bents 2 and 3, or even lower than that of OPC columns in Bent 1. This phenomenon can be attributed to the actual load on these columns. Although these two specimens, one using OPC and the other GPC, were subjected to the same excitation, the loading on each individual column was not identical. For instance, in Bent 1, the bending moment and shear force at the top of OPC columns exceeded those of the GPC columns by 15 % and 8.4 %, respectively. Consequently, the stiffer OPC columns attracted higher load, resulting in higher displacement in some cases (Bent 1).

To improve the ductility of GPC and mitigate displacements and damage levels of the GPC columns of Bents 1 and 3, incorporating fibres (e.g., steel and synthetic fibres) to the GPC mixture is a promising solution that should be considered. The effectiveness of using fibres in GPC

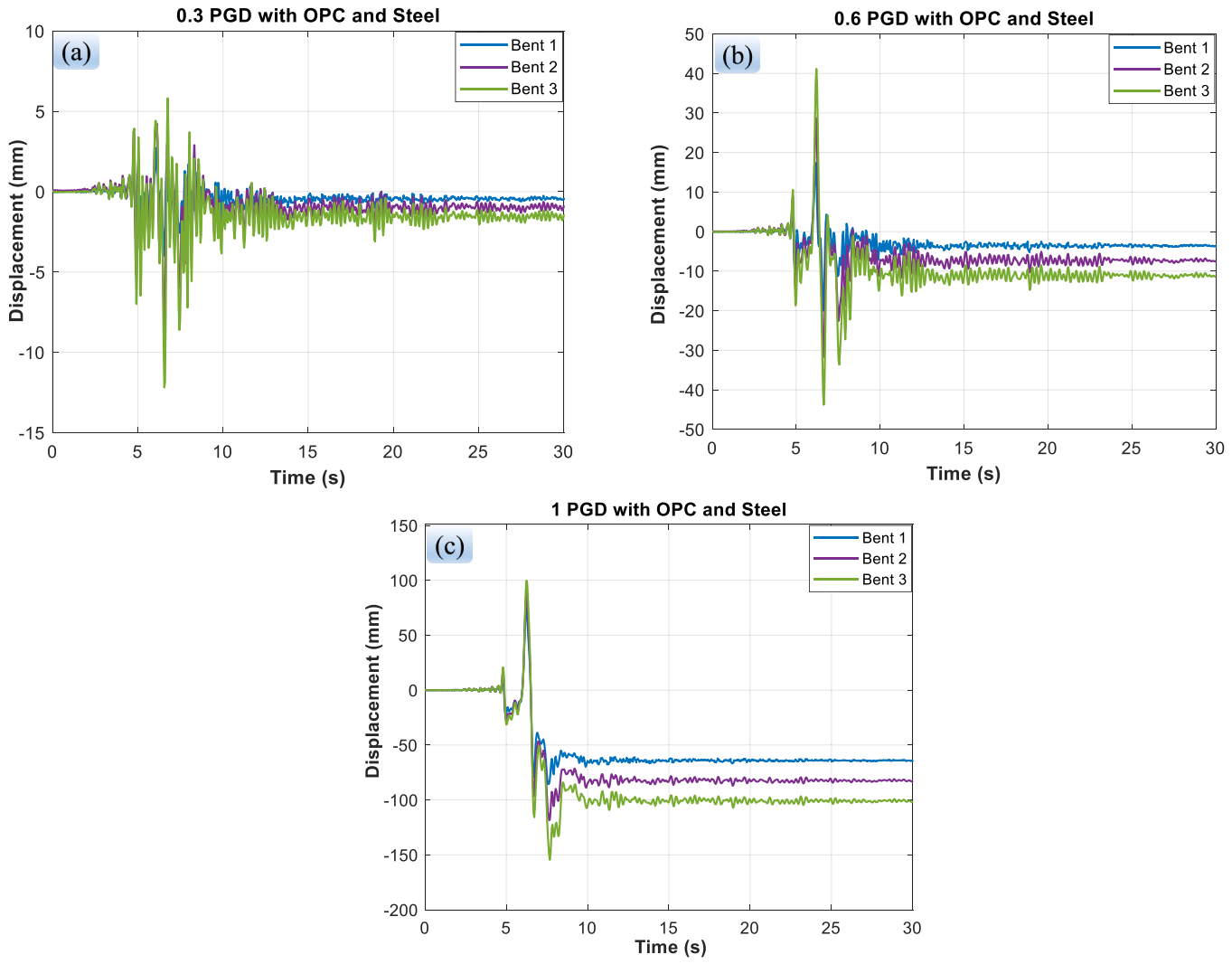

Fig. 15. Comparisons of displacement of the bents under different earthquake excitations.

mixtures has been demonstrated on beams and beam-column joints in previous studies [33,59,61,62]. In contrast, the displacements of OPC and GPC columns in Bent 2 were similar during the first 30 s because the damage level of these two columns was comparable, as shown in Fig. 11 (e) and (f). The use of GPC in Bent 2 did not significantly affect the performances of the precast bridge under seismic loads. Therefore, it could be concluded that the application of GPC caused more severe damage compared to OPC under high earthquake excitations with the combination of torsion and flexural damages. Meanwhile, when subjected to low earthquake excitations or conditions where only flexural damage is predominant, the precast bridge constructed using both GPC and OPC exhibited similar levels of damage.

4.1.2. Performances of bridge using BFRP reinforcements

The application of FRP material in construction offers several benefits as previously outlined in the introduction. However, there is currently limited number of studies investigating the performances of the FRP reinforcements and posttensioning in the precast bridge in the literature. To address this research gap, a numerical model of a precast bridge was developed by replacing all the steel reinforcements and posttensioning tendons with the BFRP reinforcements, allowing for an evaluation of the performances of BFRP-reinforced precast bridges under seismic loads, while both numerical models used OPC for a relevant comparison. The mechanical properties and material model of BFRP reinforcements are summarised in Table 4. Fig. 13 shows a comparison of displacements and failure modes between BFRP and steel reinforcements in the column of Bent 2 and Bent 3 under earthquake excitations. The trends of displacement curves and failure mode of Bent 1 and Bent 3 were similar so those of Bent 1 were not presented in Fig. 13 for brevity.

The maximum displacement and residual displacement in the columns of Bent 2 reinforced with either BFRP or steel reinforcements were almost the same at low earthquake excitation from 0 to 15 s, both reaching 13 mm and 11 mm, respectively. This is attributed to no severe damage to the columns of Bent 2 in the initial stage, where the stiffness of the bridge structure is dominated by the concrete modulus. Meanwhile, when ground excitation input increased to 1.0PGD from 15 to 30 s, the results indicated that the behaviours of Bent 2 with BFRP or steel reinforcements were significantly different. The columns with BFRP reinforcements showed higher peak and residual displacements compared to the column with steel reinforcements. For instance, in Bent 2, the maximum displacement of the columns reinforced with BFRP reinforcements was 81.4 mm, compared to 77.3 mm of the columns with steel reinforcements.

This difference could be attributed to the damage of concrete material under high excitations, making the contribution of reinforcement stiffness to the overall section stiffness of the bridge structure more prominent. Since the modulus of BFRP is smaller than that of steel, the BFRP reinforced structure therefore experienced larger displacement responses. While BFRP bars have much higher strength than that of steel

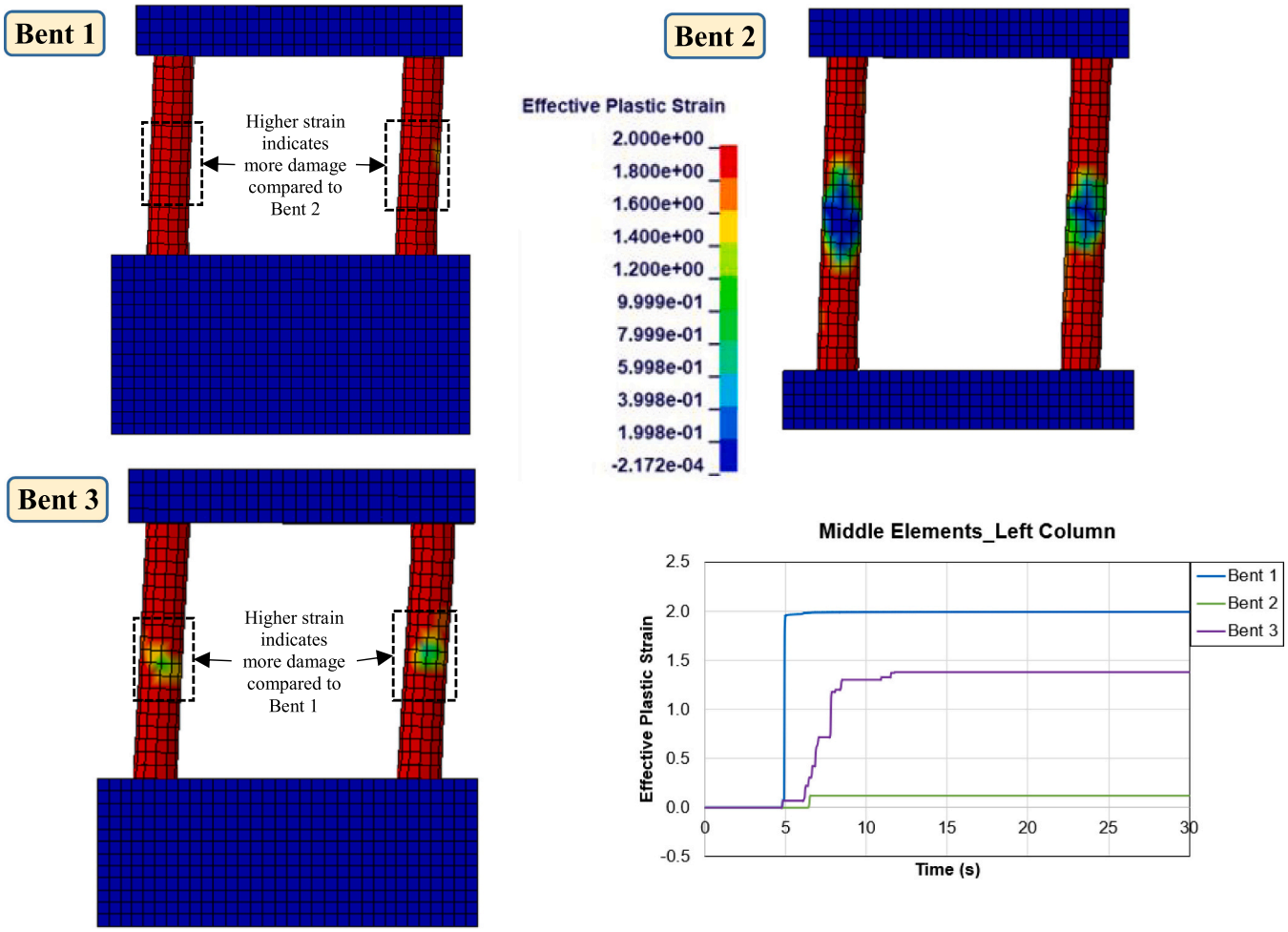

Fig. 16. Plastic deformation of the three bents under 1 PGD.

(1200 MPa vs 468 MPa), the modulus of BFRP bars was lower than that of steel bars (55 GPa vs 200 GPa). Therefore, it is not possible to achieve the same area, stiffness and strength of conventional steel reinforcements with BFRP bars simultaneously. However, a BFRP-reinforced structure can be designed to meet desired requirements. In this study, BFRP bars of similar diameter as steel bars were adopted. It is noted that a slight difference in diameter (e.g., 10 mm vs 9.5 mm) is due to the availability of these materials. To ensure the effective replacement of steel reinforcement with BFRP reinforcement, the reinforcement ratio of BFRP could be carefully considered in the design process. The damage was initially found at the top and bottom of the columns reinforced with BFRP reinforcements. Afterward, more severe damage was observed in the column using BFRP reinforcements, compared to the column reinforced with steel reinforcements (Fig. 13(c)). The column reinforced with BFRP reinforcements mainly experienced severe flexural damage.

For Bent 1 and Bent 3, the displacement of the columns reinforced with BFRP reinforcements was larger than that of the columns reinforced with steel reinforcements due to higher damage level on BFRP columns (see Fig. 13 (e) and (f)) and lower elastic modulus of BFRP reinforcements compared to steel reinforcements. The elastic modulus of BFRP reinforcements is 55 GPa which is 3.6 times lower than that of steel reinforcements (200 GPa). Lower elastic modulus results in lower stiffness of the column, leading to higher displacement of the column of Bent 3 using BFRP reinforcements, especially after the damage of concrete that reinforcements provide the primary resistance and stiffness of the column section.

4.2. *Performances of the precast bridge under near-fault fling-step motion*

The responses of the precast bridge model subjected to cross-fault ground excitations have been analyzed above. Its performances under near-fault fling-step ground excitations are examined in this section. Many recorded fling-step ground motions are available, in this study, without loss of generality, the fling-step ground motion used in Li and Bi [4] are used as input in the analysis. The subsequent sections will discuss the performances of precast bridges employing OPC, GPC, steel reinforcements, and BFRP reinforcements subjected to fling-step ground excitations. Fig. 14 shows the input data for the bridge model. It is noted that the displacement-time histories for 0.3 PGD and 0.6 PGD were derived from 1 PGD in Li and Bi [4]'s study using a scale factor. The input data gradually increases until failure occurs (i.e., 0.3, 0.6, and 1 PGD). It should be noted that owing to the lack of data, the input earthquake ground motion to the three bents was identical, i.e., the effect of ground motion spatial variation was not considered.

4.2.1. *Performances of the precast bridge using OPC and steel reinforcements*

Fig. 15 shows the displacement comparisons of Bents 1, 2 and 3 under varying earthquake excitations (i.e., 0.3, 0.6, and 1 PGD). Among the three bents, Bent 3 exhibited the greatest displacement. Specifically, under 0.6 PGD, Bent 3 reached the maximum displacement of 44 mm, while Bent 2 and Bent 1 recorded displacements of 32 and 20 mm, respectively. The discrepancy in the maximum and residual displacements between Bent 3 and Bent 1 can be attributed to their different column lengths. Bent 3 had a column length of 2020 mm, whereas Bent

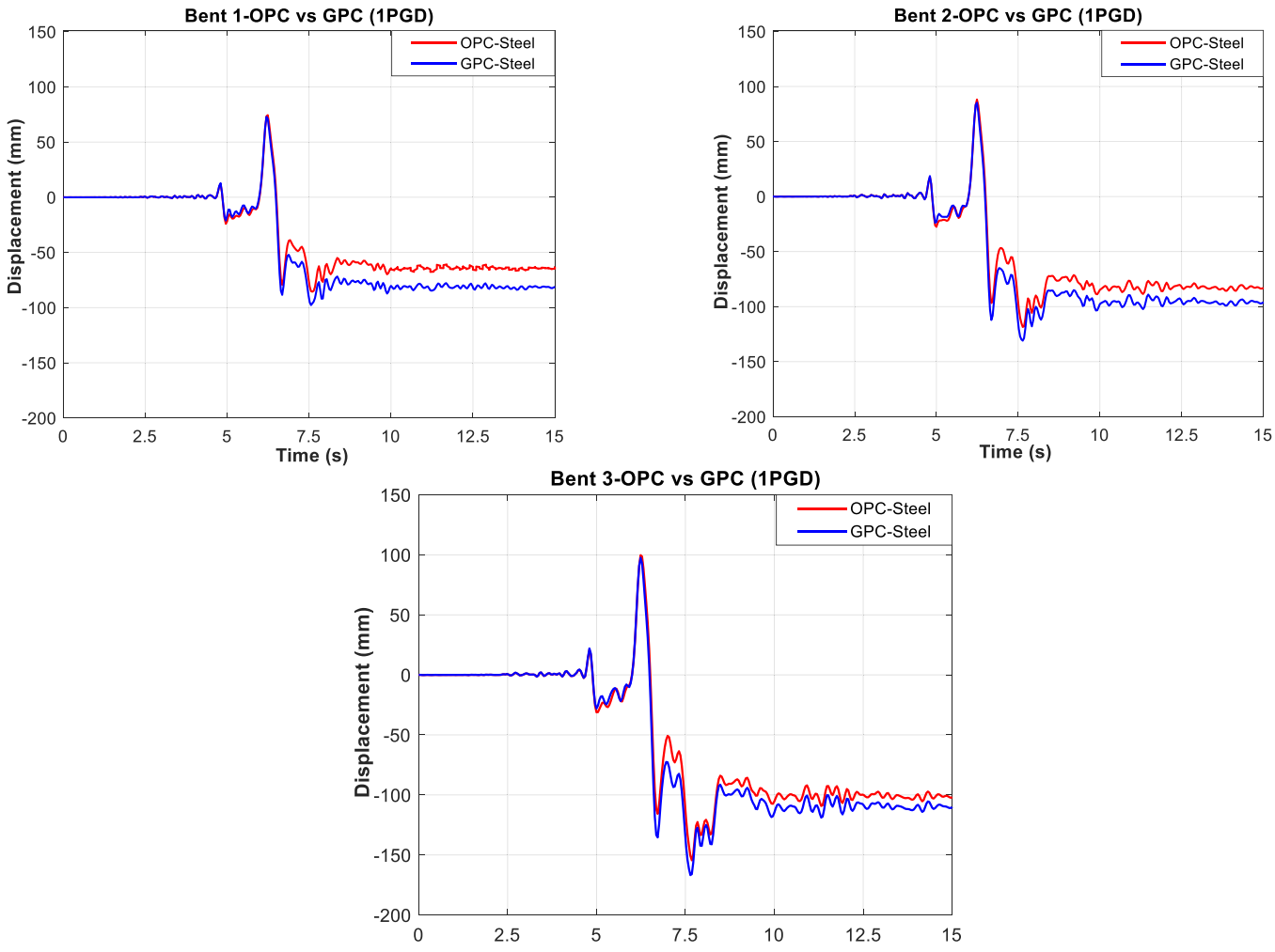

Fig. 17. Comparisons of displacements between OPC and GPC under high earthquake excitations.

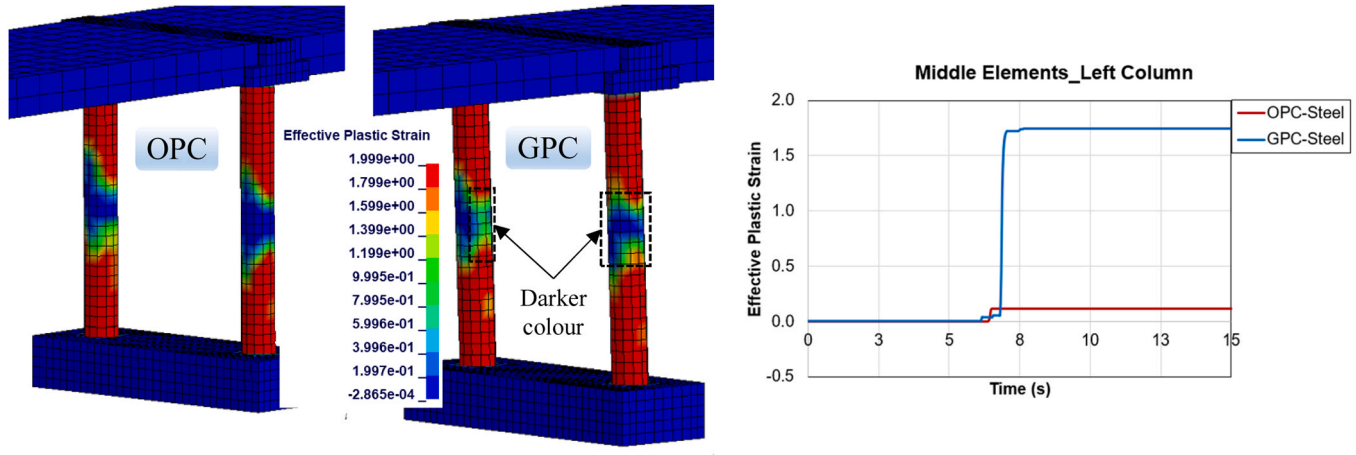

Fig. 18. Effective plastic strain of Bent 2 using OPC and GPC at 6.7 s.

1 had a length of 1710 mm, resulting in a higher displacement for Bent 3 due to its longer column length.

Interestingly, despite Bent 2 having a longer column length than Bent 3, its maximum displacement remained lower than that of Bent 3. This can be explained by the influence of constraint from Bents 1 and 3 on Bent 2. The interactions provided by the neighbouring bents limited the displacement of Bent 2 compared to Bent 3, thereby resulting in a lower displacement for Bent 2. In addition, the precast bridge experienced complete failure at 1 PGD. Severe damage was observed in all three bents as shown in Fig. 16. Flexural damage mainly governed the main failure mode of the columns. As a result, the column could not rebound back to its original position. The residual displacements of Bents 1, 2 and 3 at 1 PGD were 64, 83, and 102 mm, respectively. Consequently, the bridge suffered severe damage and ultimately failed under 1 PGD

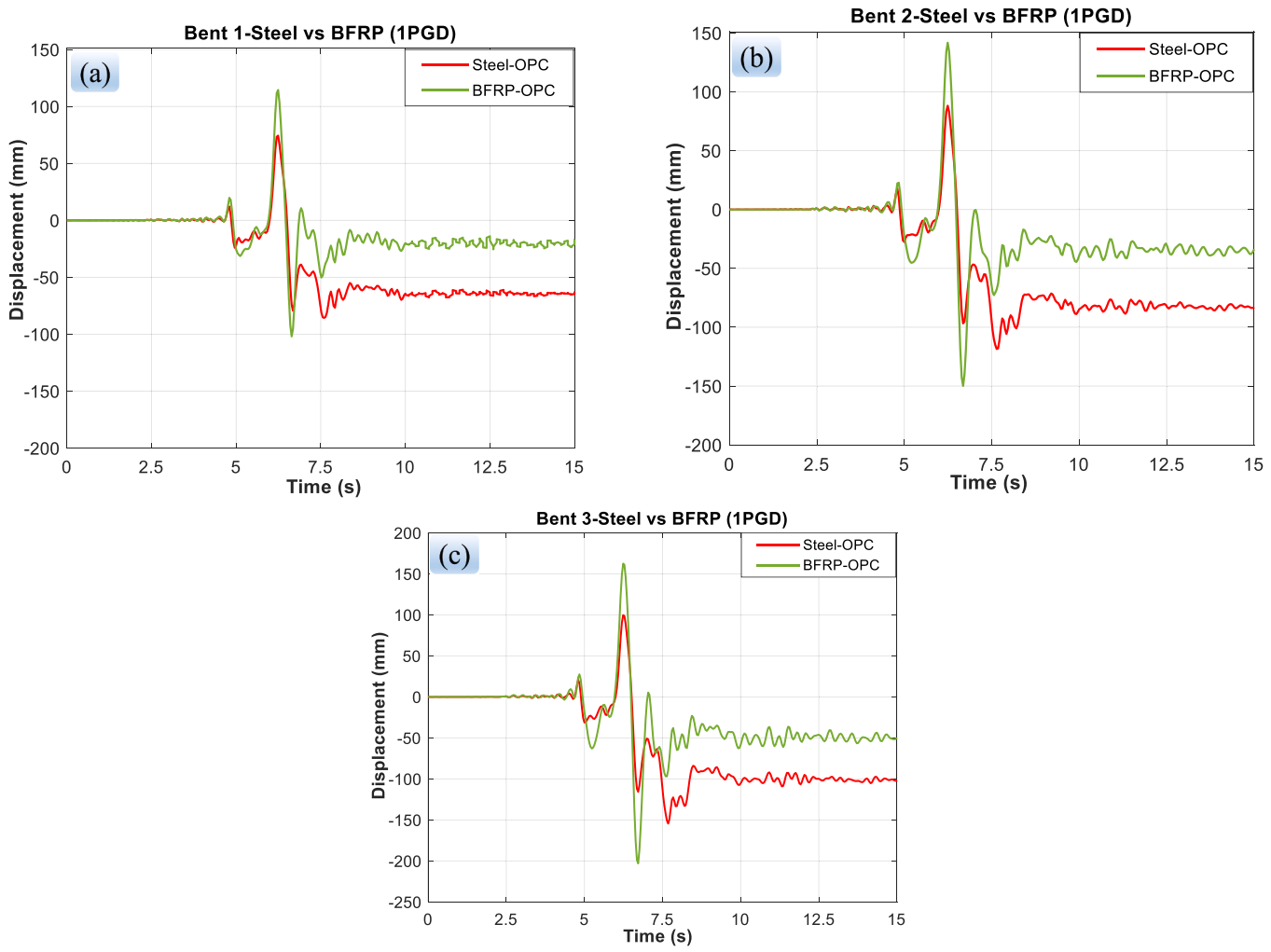

Fig. 19. Displacements of columns with BFRP vs steel reinforcements under high earthquake excitations.

excitation. It is noted that although the residual displacement of Bent 2 was higher than that of Bent 1, less damage was observed on the columns of Bent 2 compared to those of Bent 1 (see Fig. 16). This contrast can be attributed to the varied column lengths, resulting in a lower drift ratio (DR) of 3.2 % in Bent 2 in comparison to the 3.7 % drift ratio in Bent 1. In general, less damage is observed on the longer column even though its displacement is larger.

4.2.2. *Performance comparisons between OPC and GPC*

Fig. 17 shows the displacement comparisons of two bridges constructed with OPC and GPC subjected to large ground excitation with PGD equal to 810 mm. It can be observed that the maximum positive displacement at 6.2 s of both specimens was nearly identical due to similar performances of OPC and GPC under low earthquake excitation. For instance, the positive peak displacement of Bent 1 using OPC and GPC was 74 and 73 mm, respectively. However, after reaching that peak at 6.2 s, brittle failure associated with more severe damage was observed on GPC columns, compared to OPC column (see Fig. 18). Consequently, the two negative peak displacements of the GPC columns exceeded those of the OPC columns. Specifically, the two negative peak displacements of GPC columns in Bent 2 were 112 mm (4.3 % DR) and 131 mm (5 % DR), whereas those of OPC columns were 97 mm (3.7 % DR) and 119 mm (4.5 % DR), respectively. In addition, due to brittle failure and more severe damage observed in GPC columns, the residual displacement of all the three bents utilising GPC was higher than that of the bents using OPC. These findings and observations align with the results presented in Section 4.1.1 and are consistent with the findings from previous studies [32,33]. To address the brittle failure of using GPC, the application of different fibre types is a potential solution as discussed in Section 4.1.1.

4.2.3. *Performances comparison between steel and BFRP reinforcements*

Fig. 19 illustrates a comparison of the displacement between steel and BFRP columns under PGD = 810 mm. It is evident that the use of BFRP reinforcements results in higher peak displacements in all three bents compared to steel reinforcements under high PGD. For instance, the maximum displacement of the column in Bent 3 using BFRP reinforcements was 203 mm, whereas the corresponding displacement with steel reinforcements was 116 mm. This disparity in displacement was attributed to lower stiffness of BFRP columns compared to column using steel reinforcements, as explained in Section 4.1.2.

Interestingly, despite the replacement of all steel reinforcements with BFRP reinforcements and the higher peak displacements observed in BFRP columns, no brittle failure was observed in the numerical specimen. The columns utilizing BFRP reinforcements exhibited ductile behaviour with lower residual displacement under high earthquake excitation. For example, the residual displacement of the BFRP column in Bent 2 (35 mm) was 2.4 times lower than that of the steel column (85 mm). This result was attributed to the fact that the axial stress in the steel reinforcements (583 MPa) surpassed the yield stress of the longitudinal reinforcements (468 MPa) after reaching the peak displacement. Meanwhile, the column utilizing BFRP is capable of rebounding back to

its original position as depicted in Fig. 19. This favourable performance is attributed to the linear behaviour associated with high tensile strength of BFRP material until rupture. It is noted that although BFRP reinforcements did not yield under the considered ground excitations, resulting in a small residual displacement caused by damage of concrete. The above observations regarding the specimen using FRP material were aligned with a previous study [62] where ductile behaviour with very low residual displacement under impact loads was observed. This observation clearly demonstrated the advantage of employing BFRP material in structures.

5. Conclusions

The performances of the precast bridge constructed with durable FRP reinforcements and green construction materials (GPC) were investigated in this study. The main findings from the numerical investigation can be summarized as follows:

1. As compared to a more complex model, the simplified model developed in this study was able to capture the failure pattern and displacement of the precast bridge subjected to earthquake excitations with significantly reduced computational cost.
2. The developed numerical model helped to explain the reported observation which could not be explained from experimental test, e.g., the combination of torsional and flexural cracks primarily governed the main damage on the columns of Bent 1 and Bent 3, which could not be confirmed from the previous study.
3. The performances of precast bridges using ordinary Portland cement concrete (OPC) and geopolymer concrete (GPC) were similar under low ground acceleration excitations. However, under high earthquake excitations, GPC columns exhibited brittle failure with higher maximum and residual displacements, compared to OPC columns.
4. The displacements of the column using BFRP and steel reinforcements were nearly identical under low earthquake excitations. Nevertheless, the column reinforced with BFRP reinforcements showed more severe damage of concrete than the steel-reinforced column under high ground excitations.
5. The use of BFRP reinforcements showed higher peak displacements but lower residual displacements under high fling-step ground motion. The BFRP column can rebound back to its original position after intensive earthquake excitation.

In conclusion, this is the first study of investigating the performances of the precast bridges using new advanced materials (i.e., GPC and BFRP reinforcements) subjected to cross-fault and fling-step ground excitations. The performances of bridges with GPC and BFRP reinforcement are comparable to that of bridges with conventional concrete and steel reinforcement under low earthquake. However, their performance under intensive earthquake excitations showed some different behaviours which require attention of designers.

CRediT authorship contribution statement

Kaiming Bi: Writing – review & editing, Resources. **Duong T. Tran:** Writing – review & editing, Validation, Software. **Hong Hao:** Writing – review & editing, Supervision, Project administration, Funding acquisition. **Thong Pham:** Writing – review & editing, Methodology, Investigation. **Tuan T. Ngo:** Writing – original draft, Visualization, Validation, Software, Methodology, Investigation, Formal analysis, Data curation.

Declaration of Competing Interest

The authors declare no conflict of interests.

Data availability

Data will be made available on request.

Acknowledgements

The authors would like to acknowledge the financial support from the Australian Research Council Laureate Fellowships FL180100196.

References

[1] Li C, Bi K, et al. Seismic performances of precast segmental column under bidirectional earthquake motions: shake table test and numerical evaluation. Eng Struct 2019;187:314–28.
[2] Ou Y-C, Wang P-H, et al. Large-scale experimental study of precast segmental unbonded posttensioned concrete bridge columns for seismic regions. J Struct Eng 2010;136:255–64.
[3] ElGawady MA, Sha'Lan A. Seismic behavior of self-centering precast segmental bridge bents. J Bridge Eng 2011;16:328–39.
[4] Li Q, Bi K, et al. Numerical studies on the seismic responses of precast segmental columns-supported bridge structures subjected to near-fault ground motions. Adv Struct Eng 2022;25:2527–46.
[5] Bu Z-Y, Ou Y-C, et al. Cyclic loading test of unbonded and bonded posttensioned precast segmental bridge columns with circular section. J Bridge Eng 2016;21:04015043.
[6] Wang J-C, Ou Y-C, et al. Large-scale seismic tests of tall concrete bridge columns with precast segmental construction. Earthq Eng Struct Dyn 2008;37:1449–65.
[7] ElGawady M, Booker AJ, et al. Seismic behavior of posttensioned concrete-filled fiber tubes. J Compos Constr 2010;14:616–28.
[8] Marriott D, Pampanin S, et al. Quasi-static and pseudo-dynamic testing of unbonded post-tensioned rocking bridge piers with external replaceable dissipaters. Earthq Eng Struct Dyn 2009;38:331–54.
[9] Billington SL, Yoon JK. Cyclic response of unbonded posttensioned precast columns with ductile fiber-reinforced concrete. J Bridge Eng 2004;9:353–63.
[10] Feng D-C, Xu J. An efficient fiber beam-column element considering flexure–shear interaction and anchorage bond-slip effect for cyclic analysis of RC structures. Bull Earthq Eng 2018;16:5425–52.
[11] Ichikawa S, Matsuzaki H, et al. Seismic-resistant bridge columns with ultrahigh-performance concrete segments. J Bridge Eng 2016;21:04016049.
[12] Yang C, Okumus P. Ultrahigh-performance concrete for posttensioned precast bridge piers for seismic resilience. J Struct Eng 2017;143:04017161.
[13] Sideris P, Aref AJ, et al. Experimental seismic performance of a hybrid sliding–rocking bridge for various specimen configurations and seismic loading conditions. J Bridge Eng 2015;20:04015009.
[14] Sideris P, Aref AJ, et al. Large-scale seismic testing of a hybrid sliding-rocking posttensioned segmental bridge system. J Struct Eng 2014;140:04014025.
[15] Johnson N, Ranf RT, et al. Seismic testing of a two-span reinforced concrete bridge. J Bridge Eng 2008;13:173–82.
[16] Saiidi MS, Vosooghi A, et al. Shake table studies and analysis of a two-span RC bridge model subjected to a fault rupture. J Bridge Eng 2014;19:A4014003.
[17] Lin Y, Zong Z, et al. Experimental and numerical studies of the seismic behavior of a steel-concrete composite rigid-frame bridge subjected to the surface rupture at a thrust fault. Eng Struct 2020;205:110105.
[18] Tullini N, Minghini F. Grouted sleeve connections used in precast reinforced concrete construction – Experimental investigation of a column-to-column joint. Eng Struct 2016;127:784–803.
[19] Li C, Hao H, et al. Numerical study on the seismic performance of precast segmental concrete columns under cyclic loading. Eng Struct 2017;148:373–86.
[20] Le TD, Pham TM, et al. Performance of precast segmental concrete beams posttensioned with carbon fiber-reinforced polymer (CFRP) tendons. Compos Struct 2019;208:56–69.
[21] Li C, Hao H, et al. Seismic performance of precast concrete-filled circular tube segmental column under biaxial lateral cyclic loadings. Bull Earthq Eng 2019;17:271–96.
[22] Choi H. Effects of near-fault ground motion and fault-rupture on the seismic response of reinforced concrete bridges. University of Nevada, Reno; 2007.
[23] Johnson N. Large-scale experimental and analytical seismic studies of a two-span reinforced concrete bridge system. University of Nevada, Reno; 2006.
[24] Choi H, Saiidi MS, et al. Experimental study of reinforced concrete bridge columns subjected to near-fault ground motions. Acids Struct J 2010;107:3–12.
[25] Abrahamson N. Seismological aspects of near-fault ground motions. In: Proceedings of the fifth Caltrans Seismic research workshop. Sacramento, CA;1998.
[26] Zhao L, Bi K, et al. Numerical studies on the seismic responses of bridge structures with precast segmental columns. Eng Struct 2017;151:568–83.
[27] Goel RK, Chopra AK. Linear analysis of ordinary bridges crossing fault-rupture zones. J Bridge Eng 2009;14:203–15.
[28] Goel RK, Chopra AK. Nonlinear analysis of ordinary bridges crossing fault-rupture zones. J Bridge Eng 2009;14:216–24.
[29] Benhelal E, Zahedi G, et al. Global strategies and potentials to curb CO_2 emissions in cement industry. J Clean Prod 2013;51:142–61.
[30] Castel A, Foster SJ, et al. Creep and drying shrinkage of a blended slag and low calcium fly ash geopolymer Concrete. Mater Struct 2016;49:1619–28.

[31] Khan MZN, Shaikh FuA, et al. Synthesis of high strength ambient cured geopolymer composite by using low calcium fly ash. Constr Build Mater 2016;125:809–20.
[32] Ngo TT, Tran TT, et al. Performance of geopolymer concrete in monolithic and non-corrosive dry joints using CFRP bolts under cyclic loading. Compos Struct 2020:113394.
[33] Ngo T.T., Pham T.M. et al. Experimental study of a new type of hybrid joints with GFRP bolts and reinforcements under cyclic loading. Australian Earthquake Engineering Society. Mount Macedon, Victoria, Australia; 2022.
[34] Nguyen KT, Ahn N, et al. Theoretical and experimental study on mechanical properties and flexural strength of fly ash-geopolymer concrete. Constr Build Mater 2016;106:65–77.
[35] Bakharev T. Resistance of geopolymer materials to acid attack. Cem Concr Res 2005;35:658–70.
[36] Castel A, Foster SJ. Bond strength between blended slag and class F fly ash geopolymer concrete with steel reinforcement. Cem Concr Res 2015;72:48–53.
[37] Nath P, Sarker PK. Flexural strength and elastic modulus of ambient-cured blended low-calcium fly ash geopolymer concrete. Constr Build Mater 2017;130:22–31.
[38] Kitane Y, Aref AJ, et al. Static and fatigue testing of hybrid fiber-reinforced polymer-concrete bridge superstructure. J Compos Constr 2004;8:182–90.
[39] Lawler N, Polak MA. Development of FRP shear bolts for punching shear retrofit of reinforced concrete slabs. J Compos Constr 2010;15:591–601.
[40] Yunovich M, Thompson NG. Corrosion of highway bridges: economic impact and control methodologies. Concr Int 2003;25:52–7.
[41] Singh V, Bansal PP, et al. Experimental studies on strength and ductility of CFRP jacketed reinforced concrete beam-column joints. Constr Build Mater 2014;55:194–201.
[42] Agarwal BD, Broutman LJ, et al. Analysis and performance of fiber composites. John Wiley & Sons; 2017.
[43] Sharbatdar MK, Saatcioglu M, et al. Seismic flexural behavior of concrete connections reinforced with CFRP bars and grids. Compos Struct 2011;93:2439–49.
[44] Dalalbashi A, Eslami A, et al. Plastic hinge relocation in RC joints as an alternative method of retrofitting using FRP. Compos Struct 2012;94:2433–9.
[45] Li C., Bi K. et al. Comparative studies on the seismic performance of precast segmental columns with different concrete, reinforcement and tendon materials; 2024 (Under review).
[46] Huang Z, Chen W, et al. Shear behaviour of ambient cured geopolymer concrete beams reinforced with BFRP bars under static and impact loads. Eng Struct 2021;231:111730.
[47] Huang Z, Chen W, et al. Flexural behaviour of ambient cured geopolymer concrete beams reinforced with BFRP bars under static and impact loads. Compos Struct 2021;261:113282.
[48] Li H, Chen W, et al. Dynamic response of monolithic and precast concrete joint with wet connections under impact loads. Eng Struct 2022;250:113434.
[49] Li H, Chen W, et al. Influence of various impact scenarios on the dynamic performance of concrete beam-column joints. Int J Impact Eng 2022;167:104284.
[50] AASHTO I. Guide specifications for the design and construction of segmental concrete bridges. Washington: AASHTO; 1999.
[51] Officials AAoSHaT. LRFD bridge design specifications. 17th edition. Washington, D.C.: AASHTO;1998.
[52] Officials AAoSHaT. Standard specifications for highway bridges. 17th edition. Washington, D.C.: AASHTO; 2002.
[53] California_Department_of_Transportation. Seismic design criteria. Sacramento, CA; 2004.
[54] ACI 318–19. Building code requirements for structural concrete and commentary. ACI 318–19. Farmington Hills, MI 48331: ACI (American Concrete Institute); 2019. p. 503.
[55] Tran DT, Pham TM, et al. Blast behaviour of precast segmental vs monolithic concrete beams prestressed with unbonded tendons: a numerical investigation. Int J Impact Eng 2023;173:104434.
[56] Ngo TT, Pham TM, et al. Proposed new dry and hybrid concrete joints with GFRP bolts and GFRP reinforcement under cyclic loading: testing and analysis. J Build Eng 2022;49:104033.
[57] Bi K, Hao H. Numerical simulation of pounding damage to bridge structures under spatially varying ground motions. Eng Struct 2013;46:62–76.
[58] Tran DT, Pham TM, et al. Precast segmental beams made of fibre-reinforced geopolymer concrete and FRP tendons against impact loads. Eng Struct 2023;295:116862.
[59] Tran TT, Pham TM, et al. Effect of fibre reinforcements on shear capacity of geopolymer concrete beams subjected to impact load. Int J Impact Eng 2022;159:104056.
[60] Noushini A, Aslani F, et al. Compressive stress-strain model for low-calcium fly ash-based geopolymer and heat-cured Portland cement concrete. Cem Concr Compos 2016;73:136–46.
[61] Ngo TT, Pham TM, et al. Effects of steel fibres and prestress levels on behaviour of newly proposed exterior dry joints using SFRC and CFRP bolts. Eng Struct 2020;205:110083.
[62] Ngo TT, Pham TM, et al. Performance of monolithic and dry joints with GFRP bolts reinforced with different fibres and GFRP bars under impact loading. Eng Struct 2021;240:112341.